Connecting X-ray absorption and 21 cm neutral hydrogen absorption in obscured radio AGN

V. A. Moss,[1,2]★ J. R. Allison,[3] E. M. Sadler,[1,2] R. Urquhart,[4] R. Soria,[4,1,5]
J.R. Callingham,[6] S. J. Curran,[7] A. Musaeva,[1,2,3] E. K. Mahony,[1,2] M. Glowacki,[1,2,3]
S. A. Farrell,[1,2] K. W. Bannister,[3] A. P. Chippendale,[3] P. G. Edwards,[3]
L. Harvey-Smith,[3] I. Heywood,[3,8] A. W. Hotan,[3] B. T. Indermuehle,[3] E. Lenc,[1,2]
J. Marvil,[3] D. McConnell,[3] J. E. Reynolds,[3] M. A. Voronkov,[3] R. M. Wark[3]
and M. T. Whiting[3]

[1] *Sydney Institute for Astronomy, School of Physics A2, The University of Sydney, NSW 2006, Australia*
[2] *ARC Centre of Excellence for All-Sky Astrophysics (CAASTRO)*
[3] *CSIRO Astronomy and Space Science, ATNF, PO Box 76, Epping, NSW 1710, Australia*
[4] *International Centre for Radio Astronomy Research, Curtin University, GPO Box U1987, Perth, WA 6845, Australia*
[5] *National Astronomical Observatories, Chinese Academy of Sciences, Beijing 100012, China*
[6] *ASTRON, the Netherlands Institute for Radio Astronomy, PO Box 2, NL-7990 AA Dwingeloo, the Netherlands*
[7] *School of Chemical and Physical Sciences, Victoria University of Wellington, PO Box 600, Wellington 6140, New Zealand*
[8] *Department of Physics and Electronics, Rhodes University, PO Box 94, Grahamstown 6140, South Africa*

ABSTRACT

Many radio galaxies show the presence of dense and dusty gas near the active nucleus. This can be traced by both 21 cm H I absorption and soft X-ray absorption, offering new insight into the physical nature of the circumnuclear medium of these distant galaxies. To better understand this relationship, we investigate soft X-ray absorption as an indicator for the detection of associated H I absorption, as part of preparation for the First Large Absorption Survey in H I to be undertaken with the Australian Square Kilometre Array Pathfinder (ASKAP). We present the results of our pilot study using the Boolardy Engineering Test Array, a precursor to ASKAP, to search for new absorption detections in radio sources brighter than 1 Jy that also feature soft X-ray absorption. Based on this pilot survey, we detected H I absorption towards the radio source PKS 1657−298 at a redshift of $z = 0.42$. This source also features the highest X-ray absorption ratio of our pilot sample by a factor of 3, which is consistent with our general findings that X-ray absorption predicates the presence of dense neutral gas. By comparing the X-ray properties of active galactic nuclei with and without detection of H I absorption at radio wavelengths, we find that X-ray hardness ratio and H I absorption optical depth are correlated at a statistical significance of 4.71σ. We conclude by considering the impact of these findings on future radio and X-ray absorption studies.

Key words: methods: observational – galaxies: active – galaxies: ISM – galaxies: nuclei – radio lines: galaxies – X-rays: galaxies.

1 INTRODUCTION

The cores of active galaxies produce emission across the electromagnetic spectrum, with each wavelength opening a different window into the nature of the supermassive black holes at their centre and their surrounding medium (Heckman & Best 2014; Tadhunter 2016, and references therein). Many compact active galactic nuclei (AGN) detected at radio wavelengths are also X-ray bright, and the X-ray emission observed can be produced via a number of different mechanisms, such as the inner accretion flow (either an advection-dominated region or a hot corona above the inner disc and its reflected component), directly from the jet (synchrotron emission) or from the interaction of the jet with the

★ E-mail: vanessa.moss@sydney.edu.au

surrounding medium (hot thermal-plasma emission), amongst other processes (see e.g. Haardt & Maraschi 1993; Merloni, Heinz & Di Matteo 2003; Turner & Miller 2009; Worrall 2009; Fabian 2012; Reynolds 2016).

Previous studies investigating X-ray and radio AGN have included comparison of the column densities estimated from 21 cm neutral atomic hydrogen (H I) absorption (N_{HI}, assuming a spin temperature) and an absorbed X-ray spectrum (N_H, the combination of ionized, neutral and molecular hydrogen), finding a weak correlation between these two properties (e.g. Vink et al. 2006; Ostorero et al. 2010). This in turn indicates likely spatial correlation between these different wavelength tracers of gas near the AGN, although their exact relationship is of ongoing consideration as the X-ray emission most likely originates close to the central black hole while the radio emission can be more extended (Vink et al. 2006). A specific focus has been on the gigahertz-peaked spectrum (GPS) and compact steep spectrum (CSS) radio sources, as these are believed to represent the early stages of AGN evolution (Fanti et al. 1995; O'Dea 1998; Tinti & De Zotti 2006; Siemiginowska et al. 2008). This has been supplemented by studies showing a higher detection rate of H I in these kinds of galaxies, particularly in the local Universe (e.g. Gereb et al. 2015; Maccagni et al. 2017). However, different processes may dominate in particular AGN depending on their accretion rates, jet power, density of the surrounding medium and, importantly, evolutionary age.

By investigating the connection between the X-ray properties, radio emission and H I absorption, we can build up a better understanding of how these various factors influence the resulting observed properties and consequent evolution of galaxies. Thus, our study extends beyond the youngest radio AGN to the correlation between X-rays and radio in AGN of all types. We are particularly interested in tracing the gas of galaxies, as gas content across cosmic time-scales is a key factor in the question of overall evolution of the baryonic Universe. Results show that the gas reservoir has decreased to present day (Noterdaeme et al. 2012; Curran 2017), with the overall state of galaxies becoming more quiescent alongside a decrease in the star formation rate (Madau & Dickinson 2014). H I absorption studies offer a unique glimpse into these gaseous galaxies along a sightline to the often-compact background radio emission, revealing gas that is 'censored' by the size of the radio source. The gas illuminated by these studies is generally found to trace circumnuclear discs, but can also reveal outflow and infall processes (Morganti, Sadler & Curran 2015, and references therein). A key advantage is the ability to detect neutral hydrogen gas independent of redshift, in contrast to studies of H I emission.

The First Large Absorption Survey in H I (FLASH, Sadler et al. in preparation) will be the first blind southern all-sky survey for H I absorption. It will be performed by the Australian Square Kilometre Array Pathfinder (ASKAP, Johnston et al. 2007), which features instantaneous 300 MHz bandwidth and a 5×5 deg field of view. ASKAP will be able to efficiently search the redshift range $0.4 < z < 1.0$ for 21 cm H I absorption towards over 150 000 background galaxies, in a single frequency band covering frequencies of 700–1000 MHz with little impact from radio frequency interference (RFI) due to its radio-quiet host site at the Murchison Radio-astronomy Observatory. Until 2016 February, the ASKAP instrument operated in commissioning mode as a six-antenna prototype interferometer known as the Boolardy Engineering Test Array (BETA, Hotan et al. 2014; McConnell et al. 2016). A map of BETA baselines, including the numbering of relevant antennas, is shown in Fig. 1. Despite its modest sensitivity, BETA has already highlighted the scope for exploration of H I in this unique
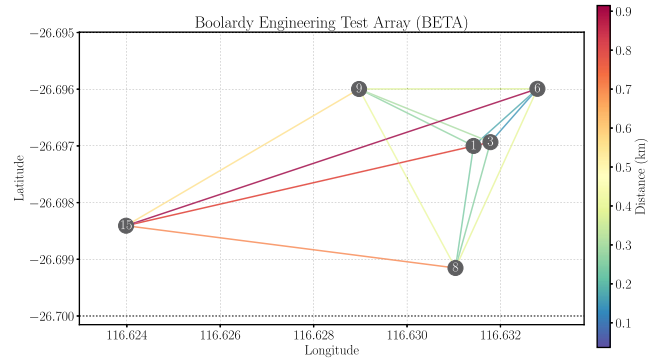
Figure 1. Baseline map of BETA, a six-antenna precursor interferometer for ASKAP which was in operation until 2016 February. The baseline lengths are colour-coded by distance, ranging from 37–915 m. For more details about the BETA instrument and baseline properties, see Hotan et al. (2014).

parameter space with the discovery of associated H I absorption towards PKS 1740−517 at $z = 0.44$ (Allison et al. 2015, 2016). PKS 1740−517 presented a particularly interesting case study given its diverse multi-wavelength properties. It features a hard X-ray spectrum that is absorbed at the soft end (<2 keV), suggesting the presence of dense hydrogen along the line of sight to the source of X-ray emission. We focus here on further investigating this connection between H I absorption and soft X-ray absorption in radio galaxies.

We consider in this paper the X-ray properties of PKS 1740−517 alongside other known H I absorbing sources in associated systems. We compare the properties of these systems to galaxies with non-detections of H I absorption that also feature X-ray emission. We also report on the results of the pilot study we have carried out using BETA to target radio-bright, absorbed X-ray sources. We report on our new detection of H I absorption towards PKS 1657−298 and discuss the multi-wavelength properties of this radio source. Finally, we summarize our findings and speculate on the future potential for using X-ray spectral information in the context of informing FLASH and other searches for H I absorption.

2 X-RAY PROPERTIES OF AGN WITH KNOWN H I ABSORPTION AND H I NON-DETECTIONS

To examine the connection between H I absorption and the properties of associated X-ray emission, we considered both sources with known H I absorption and sources which had been searched for H I absorption with no resulting detection. We refer throughout the paper to sources without a detection as either non-detections or non-absorbers, but stress that they are only non-absorbing at the limit of current observations. Our list of associated systems that have been searched for H I absorption was adapted from a compilation maintained from the literature (see Curran & Whiting 2010, for an earlier version). We note that we do not consider intervening systems here, as we are interested in the properties of neutral gas in radio AGN hosts and so the H I should be associated with the AGN rather than along the line of sight. We also exclude the BETA sample described later in this paper, given the lack of complete redshift information. We cross-matched the list of absorbers and non-detections against the 3XMM-DR4 catalogue (Rosen et al. 2015), resulting in a total of 20 H I absorbers and 74 non-H I absorbers with corresponding X-ray emission. A list of these 94 sources and their properties is given in Table 1. The median separation between the radio and X-ray sources was 0.4 arcsec, which is well within the average positional

Table 1. Properties of our sample of 94 AGN with catalogued X-ray emission in the XMM-DR4 catalogue (Rosen et al. 2015) that either have detected H I absorption or have been searched for H I absorption with no detection. The overall compilation of H I absorbers and non-absorbers was adapted from a list maintained from the literature (see e.g. Curran & Whiting 2010). We note that N_{HI} is calculated assuming a covering fraction f of 1 and a spin temperature T_s of 100 K. The variables f_1 and f_5 refer to the fluxes in Band 1 (0.2–0.5 keV) and Band 5 (4.5–12 keV) of 3XMM-DR4, respectively. Uncertainties in values are implicit in the significant figures.

	Source	H I	RA J2000	Dec. J2000	z	N_{HI} $(10^{20}$ cm$^{-2})$	τ	Ref.	f_1 $(10^{-14}$ mW m$^{-2})$	f_5 $(10^{-14}$ mW m$^{-2})$	$\frac{f_5}{f_1}$
1	NGC 0315	Y	00:57:48.88	+30:21:08.82	0.016	6.9	0.05	E10	3.70	46.63	13
2	CGRaBS J0111+3906	Y	01:11:37.32	+39:06:28.12	0.668	22.9	0.44	O06	0.02	3.89	219
3	NGC 1167	Y	03:01:42.37	+35:12:20.66	0.016	1.2	0.0023	E10	0.31	0.69	2
4	PKS 0428+20	Y	04:31:03.76	+20:37:34.25	0.219	3.5	0.0445	V03	0.04	1.23	34
5	PKS 0500+019	Y	05:03:21.20	+02:03:04.68	0.585	6.2	0.045	C98	0.28	26.87	95
6	2MFGC 06756	Y	08:34:54.90	+55:34:21.07	0.242	1.1	0.0032	V03	29.85	217.16	7
7	B2 0902+34	Y	09:05:30.10	+34:07:56.93	3.398	3.1	0.011	U91	0.09	2.80	33
8	J125711−172434	Y	12:57:11.59	−17:24:33.98	0.048	33.9	0.1	G17	0.65	0.49	1
9	NGC 5090	Y	13:21:12.82	−43:42:16.38	0.011	2.7	0.029	M01	2.23	33.09	15
10	4C +32.44	Y	13:26:16.51	+31:54:09.50	0.370	0.7	0.00268	V03	0.64	5.15	8
11	NGC 5363	Y	13:56:07.21	+05:15:17.17	0.004	11.2	0.039	V89	1.30	8.88	7
12	4C +62.22	Y	14:00:28.65	+62:10:38.60	0.431	1.9	0.00741	V03	0.12	27.95	232
13	MRK 0668	Y	14:07:00.39	+28:27:14.69	0.077	1.8	0.00433	V03	0.93	27.94	30
14	PKS 1549−79	Y	15:56:58.87	−79:14:04.27	0.150	3.6	0.026	M01	0.42	490.84	1167
15	3C 353	Y	17:20:28.16	−00:58:46.63	0.030	41.7	0.109	M01	0.07	83.78	1123
16	PKS 1740−517	Y	17:44:25.39	−51:44:44.70	0.441	5.0	0.2026	A15	0.01	69.30	8689
17	PKS 1814−63	Y	18:19:35.00	−63:45:48.20	0.065	24.0	0.192	A12	0.41	313.18	770
18	3C 452	Y	22:45:48.77	+39:41:16.01	0.081	6.5	0.058	C13	0.37	235.38	641
19	3C 459	Y	23:16:35.23	+04:05:18.06	0.220	0.7	0.00311	V03	0.67	7.65	11
20	COINS J2355+4950	Y	23:55:09.46	+49:50:08.34	0.238	2.8	0.018	V03	0.03	6.00	188
21	NGC 0383	N	01:07:24.96	+32:24:45.22	0.017	<0.6	<0.003	E10	2.36	3.94	2
22	J011132−730209	N	01:11:32.25	−73:02:09.89	0.067	<7.8	−	G17	0.07	9.13	122
23	UGC 01651	N	02:09:38.53	+35:47:51.07	0.038	<0.5	<0.003	E10	0.94	1.64	2
24	3C 066A	N	02:22:39.61	+43:02:07.80	0.444	<0.5	−	G+	36.04	89.11	2
25	UGC 01841	N	02:23:11.41	+42:59:31.38	0.021	<3.8	<0.0195	C13	4.40	9.69	2
26	3C 067	N	02:24:12.30	+27:50:11.54	0.310	<1.4	<0.008	V03	1.28	30.28	24
27	[HB89] 0235+164	N	02:38:38.93	+16:36:59.29	0.940	<1.3	−	G+	7.66	144.75	19
28	[HB89] 0237−233	N	02:40:08.17	−23:09:15.73	2.223	<0.2	−	G+	22.30	116.81	5
29	B3 0309+411B	N	03:13:01.96	+41:20:01.18	0.134	<1.7	<0.0087	C13	13.44	203.40	15
30	ESO 248−G006	N	03:17:57.67	−44:14:17.45	0.076	<0.6	<0.01	A12	233.57	918.64	4
31	NGC 1275	N	03:19:48.16	+41:30:42.12	0.018	−	−	G+	968.10	10 082.00	10
32	UGC 02748	N	03:27:54.19	+02:33:41.98	0.030	<1.5	<0.028	M01	0.25	12.75	51
33	J033114−524148	N	03:31:14.99	−52:41:48.19	0.067	<15.8	−	G17	1.38	10.00	7
34	3C 111	N	04:18:21.28	+38:01:35.80	0.049	<0.4	<0.002	C13	10.65	3865.50	363
35	J043022−613201	N	04:30:22.00	−61:32:01.00	0.056	<3.2	−	G17	4.03	5.75	1
36	3C 120	N	04:33:11.10	+05:21:15.62	0.033	<0.4	<0.006	V89	222.42	3263.90	15
37	ESO 362−G021	N	05:22:57.98	−36:27:30.85	0.057	<0.1	<0.013	V89	125.94	612.09	5
38	[HB89] 0537−286	N	05:39:54.28	−28:39:55.94	3.014	<2.8	<0.1	C08	14.87	243.07	16
39	[HB89] 0552+398	N	05:55:30.81	+39:48:49.18	2.365	<1.7	−	G+	1.66	116.97	71
40	3C 153	N	06:09:32.51	+48:04:15.38	0.277	<0.6	<0.003	V03	0.99	0.00	0
41	PKS 0625−35	N	06:27:06.76	−35:29:15.25	0.055	<0.4	<0.007	M01	112.89	152.73	1
42	4C +43.15	N	07:35:21.89	+43:44:20.33	2.429	−	<0.004	R99	0.10	1.53	15
43	B2 0738+31	N	07:41:10.70	+31:12:00.22	0.631	<2.4	−	G+	5.72	40.14	7
44	CGCG 262−029	N	07:48:36.87	+55:48:58.25	0.036	<2.8	<0.0054	C13	0.13	0.10	1
45	NGC 2484	N	07:58:28.11	+37:47:11.80	0.043	<3.2	<0.0165	C13	3.92	9.02	2
46	3C 192	N	08:05:35.00	+24:09:50.33	0.060	<0.4	<0.002	G06	0.60	23.44	39
47	3C 207	N	08:40:47.59	+13:12:23.58	0.681	<0.5	<0.003	V03	10.62	120.48	11
48	[HB89] 0836+710	N	08:41:24.36	+70:53:42.18	2.172	−	−	G+	190.20	2687.80	14
49	OJ +287	N	08:54:48.88	+20:06:30.64	0.306	−	−	G+	31.00	139.49	4
50	PKS 0921−213	N	09:23:38.88	−21:35:47.11	0.052	<3.5	<0.059	A12	75.21	488.68	6
51	[HB89] 0954+658	N	09:58:47.24	+65:33:54.83	0.368	<1.4	−	G+	20.27	171.29	8
52	SDSS J103507.04+562846.8	N	10:35:07.04	+56:28:46.81	0.459	<1.3	<0.007	V03	0.08	4.40	55
53	[HB89] 1055+018	N	10:58:29.61	+01:33:58.82	0.888	<0.5	−	G+	34.41	162.56	5
54	MRK 0421	N	11:04:27.31	+38:12:31.79	0.030	<0.4	<0.006	V89	7841.50	4457.70	1
55	4C +14.41	N	11:20:27.81	+14:20:55.00	0.362	<0.6	<0.003	V03	0.19	2.01	11
56	NGC 3665	N	11:24:43.67	+38:45:46.26	0.007	<20.0	<0.11	E10	6.31	9.01	1
57	NGC 3862	N	11:45:05.01	+19:36:22.75	0.022	<0.6	<0.008	V89	51.71	66.40	1
58	NGC 4278	N	12:20:06.82	+29:16:50.74	0.002	<0.3	<0.0015	E10	45.14	123.81	3
59	FBQS J1221+3010	N	12:21:21.94	+30:10:37.09	0.184	<7.9	<0.044	G15	1449.50	1269.30	1

Table 1 – continued.

	Source	H I	RA J2000	Dec. J2000	z	N_{HI} $(10^{20}$ cm$^{-2})$	τ	Ref.	f_1 $(10^{-14}$ mW m$^{-2})$	f_5 $(10^{-14}$ mW m$^{-2})$	$\frac{f_5}{f_1}$
60	B2 1219+28	N	12:21:31.69	+28:13:58.51	0.102	<1.2	–	G+	194.43	107.34	1
61	3C 273	N	12:29:06.70	+02:03:08.60	0.158	–	–	G+	1465.90	6569.30	4
62	MESSIER 087	N	12:30:49.42	+12:23:28.03	0.004	<0.7	<0.007	V89	974.97	1126.20	1
63	NGC 4696	N	12:48:49.25	−41:18:38.99	0.010	<0.5	<0.009	M01	117.31	385.18	3
64	3C 279	N	12:56:11.17	−05:47:21.52	0.536	<0.1	–	G+	108.38	573.47	5
65	[HB89] 1308+326	N	13:10:28.66	+32:20:43.80	0.996	–	–	G+	48.60	307.76	6
66	3C 287	N	13:30:37.69	+25:09:10.87	1.055	<0.1	–	G+	8.04	26.19	3
67	IC 4296	N	13:36:39.03	−33:57:56.99	0.012	<2.2	<0.041	M01	4.01	60.66	15
68	IC 4374	N	14:07:29.76	−27:01:04.30	0.022	<1.2	<0.017	V89	4.23	8.25	2
69	3C 303.1	N	14:43:14.56	+77:07:27.70	0.267	<1.4	<0.008	V03	0.18	1.47	8
70	B3 1445+410	N	14:47:12.76	+40:47:44.95	0.195	<1.1	<0.006	G15	1.22	0.83	1
71	CGCG 021−063	N	15:16:40.22	+00:15:01.91	0.052	<0.5	<0.0028	G06	18.67	136.99	7
72	3C 318	N	15:20:05.45	+20:16:05.77	1.574	<0.1	–	G+	1.34	10.17	8
73	2MASX J15320226+3016290	N	15:32:02.24	+30:16:28.96	0.065	<11.7	<0.064	G15	31.36	39.49	1
74	NGC 6166	N	16:28:38.48	+39:33:05.62	0.030	<3.7	<0.0192	C13	410.26	1299.10	3
75	NGC 6251	N	16:32:31.97	+82:32:16.40	0.025	<1.0	<0.013	V89	32.04	255.84	8
76	PKS 1637−77	N	16:44:16.12	−77:15:48.82	0.043	<2.6	<0.047	M01	13.11	102.20	8
77	MRK 0501	N	16:53:52.22	+39:45:36.61	0.034	<1.7	<0.023	V89	760.76	1051.70	1
78	B3 1702+457	N	17:03:30.38	+45:40:47.17	0.060	<4.2	<0.0229	C11	286.77	424.09	1
79	CGCG 173−014	N	18:35:03.39	+32:41:46.79	0.058	<2.8	<0.0147	C13	558.51	2492.80	4
80	3C 390.3	N	18:42:08.99	+79:46:17.11	0.056	<4.0	<0.0189	C13	419.80	2784.60	7
81	PKS 2000−330	N	20:03:24.12	−32:51:45.14	3.773	<9.5	–	G+	3.76	36.83	10
82	PKS 2008−068	N	20:11:14.22	−06:44:03.55	0.547	<0.3	–	G+	0.02	2.22	123
83	PKS 2126−15	N	21:29:12.18	−15:38:41.03	3.268	<3.6	–	G+	30.34	656.24	22
84	PKS 2135−20	N	21:37:50.01	−20:42:31.68	0.635	<1.1	<0.006	V03	0.32	3.12	10
85	ESO 075−G041	N	21:57:05.98	−69:41:23.68	0.028	<0.6	<0.01	M01	106.87	443.52	4
86	BL Lac	N	22:02:43.29	+42:16:39.97	0.069	<0.7	<0.009	V89	18.46	489.17	26
87	[HB89] 2201+315	N	22:03:14.98	+31:45:38.27	0.295	<0.5	–	G+	47.85	311.95	7
88	J220538−053531	N	22:05:38.59	−05:35:31.88	0.057	<9.8	–	G17	37.20	76.99	2
89	3C 445	N	22:23:49.53	−02:06:12.85	0.056	<2.4	<0.008	M01	4.32	684.11	158
90	3C 454	N	22:51:34.74	+18:48:40.10	1.757	<0.2	–	G+	2.07	11.89	6
91	3C 454.3	N	22:53:57.75	+16:08:53.56	0.859	<0.1	–	G+	61.42	902.88	15
92	IC 1459	N	22:57:10.61	−36:27:43.99	0.006	<0.7	<0.009	V89	7.77	47.53	6
93	MCG −07 − 47 −031	N	23:19:05.91	−42:06:48.20	0.055	<2.2	<0.038	A12	68.45	89.42	1
94	NGC 7720	N	23:38:29.39	+27:01:53.26	0.030	<3.2	<0.0162	C13	1.10	2.19	2

References: V89 (van Gorkom et al. 1989), U91 (Uson, Bagri & Cornwell 1991), C98 (Carilli et al. 1998), R99 (Röttgering, de Bruyn & Pentericci 1999), M01 (Morganti et al. 2001), V03 (Vermeulen et al. 2003), G06 (Gupta et al. 2006), O06 (Orienti, Morganti & Dallacasa 2006), C08 (Curran et al. 2008), E10 (Emonts et al. 2010), C11 (Chandola, Sirothia & Saikia 2011), A12 (Allison et al. 2012), C13 (Chandola, Gupta & Saikia 2013), G15 (Gereb et al. 2015), G+ (Grasha et al, in prep), G17 (Glowacki et al. 2017).

offsets in 3XMM-DR4 of ∼1–2 arcsec when compared with the verified Sloan Digital Sky Survey counterparts (Rosen et al. 2015).

2.1 Results of population comparison

In order to characterize the X-ray spectral energy distribution, we plotted the spectral shape of both populations as given by the 3XMM-DR4 catalogue in each of the five bands of *XMM–Newton* (0.2–0.5 keV, 0.5–1.0 keV, 1.0–2.0 keV, 2.0–4.5 keV and 4.5–12 keV, corresponding to bands f_1 to f_5). Each spectrum is normalized by its catalogued total flux (f_8, 0.2–12 keV), in order to aid comparison and reduce scatter. In this paper, we define X-ray hardness ratio as the ratio of the 4.5–12 keV band over the 0.2–0.5 keV band, specified by $\frac{f_5}{f_1}$. The results are shown in Fig. 2, for both the H I absorbers (top) and the H I non-detections (bottom), with the normalized fluxes plotted at the position of the upper limit of each band. The median and mean spectra for both samples are shown in Fig. 3, compared with the median and mean spectrum for the overall 3XMM-DR4 source population in black to highlight the difference in the two populations. The population of H I absorbers

generally features absorbed spectra (indicated by the missing soft X-ray flux at the low energy end) and less scatter in flux prior to normalization. Conversely, the non-absorbers feature flatter spectra and a much larger scatter in flux distribution before normalizing. The effect of redshift has not been included in the plotted figures. Including this effect would shift the spectra left towards lower energies and affect the flux scale, but is most relevant only for sources with $z > 1$ (a small fraction of our sample). Under the assumption that we are dealing with sources featuring simple power laws, which is true in the majority of cases, then this does not have a significant impact on the measured ratio of $\frac{f_5}{f_1}$.

We also consider the relationship between X-ray ratio and the chance of a detection of H I absorption. Fig. 4 shows 21 cm optical depth τ (either the peak τ of an absorber or the upper limit on a non-absorber) versus X-ray hardness ratio for a reduced sample of 67 galaxies (those for which we have measured 21 cm optical depths or upper limits). As the X-ray hardness ratio increases, the fraction of galaxies that have H I absorption also increases from 0.1 to 1 (shown as text labels in the figure, although it is relatively small number statistics at the high end). To characterize the trends
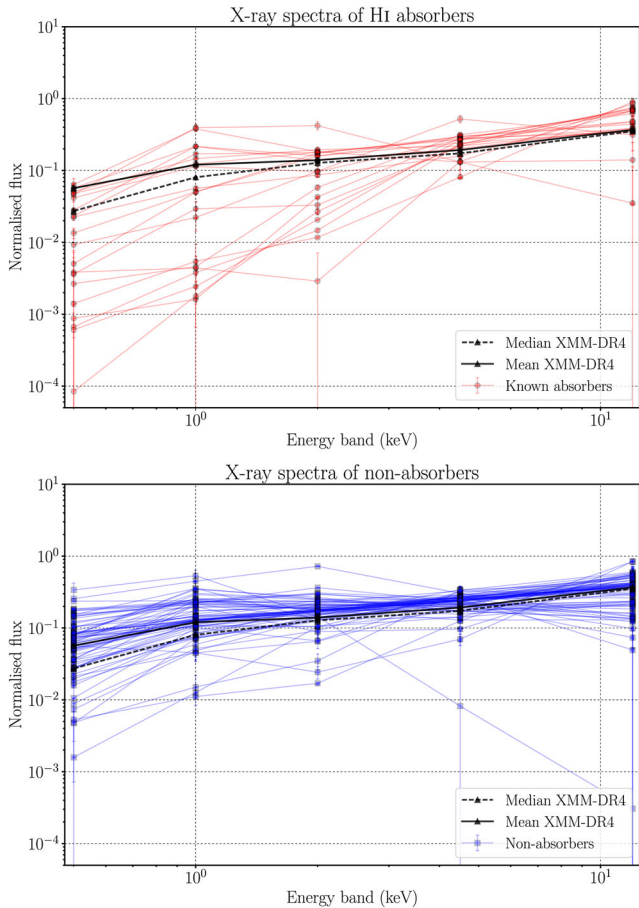
Figure 2. 3XMM-DR4 spectral properties for all galaxies with known H I detections (top, red) and those with no detection of H I absorption (bottom, blue), shown on the same axes. The fluxes have been normalized by the catalogued flux for the whole band (f_8, 0.2–12 keV) to minimize the effect of scatter. The population of H I absorbers generally features absorbed spectra (indicated by the missing soft X-ray flux at lower energies) and less scatter in flux prior to normalization. Conversely, the non-absorbers feature flatter spectra and a much larger scatter in flux distribution before normalizing. We show the median and mean spectra for all catalogued 3XMM-DR4 sources in black.

in each population, we carried out survival analysis (Feigelson & Nelson 1985; Isobe, Feigelson & Nelson 1986) on the reduced sample of 67 galaxies. A generalized non-parametric Kendall-tau test (where tau here is distinct from optical depth τ) on the detected 21 cm points gives a probability of $P(\tau) = 2.30 \times 10^{-3}$ of the distribution occurring by chance, which is significant at $S(\tau) = 3.04\sigma$ assuming Gaussian statistics. We can include the upper limits to the optical depths, from the non-detections, via the *Astronomy SUR-Vival Analysis* (ASURV) package (Isobe, Feigelson & Nelson 1986; Lavalley, Isobe & Feigelson 1992). We note that these upper limits represent the 3σ confidence interval. These are added to the 20 detected sightlines as censored data points, giving $P(\tau) = 2.38 \times 10^{-6}$ for the whole sample, which is significant at $S(\tau) = 4.71\sigma$. Thus, the data indicates a strong correlation between the optical depth and the X-ray hardness ratio. We plot these data, as well as the fits determined by the survival analysis, in Fig. 4. We show a similar plot, but for radio continuum flux instead of optical depth, in Fig. 5. This figure includes all of our 94 galaxy sample, as well as our pilot BETA sample (shown as orange triangles). The fraction of H I absorbers in each order-of-magnitude bin is again shown but for
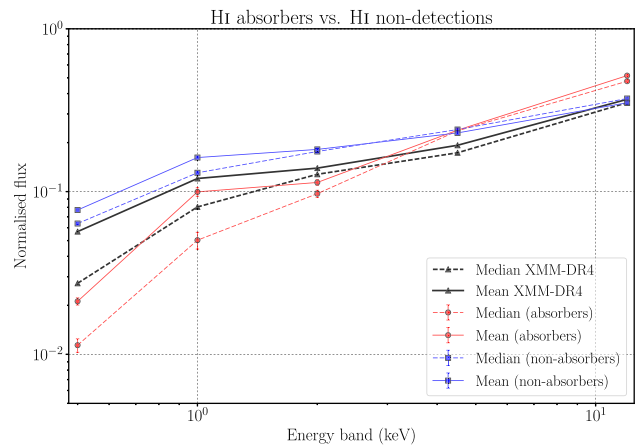
Figure 3. The median and mean spectra for H I absorbers (red) and H I non-absorbers (blue) compared with the overall distribution of all X-ray sources (black). As in the previous figure, fluxes have been normalized by the catalogued flux for the whole band (f_8, 0.2–12 keV) to minimize the effect of scatter. This highlights the more absorbed X-ray spectrum that is common to known H I absorbers versus the relative flatness of non-absorber X-ray spectra. The median and mean spectra for all 3XMM-DR4 sources are shown in black.
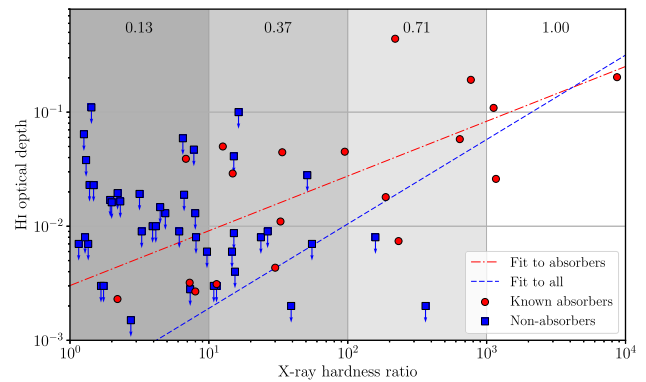
Figure 4. Optical depth τ (or 3σ upper limit on τ for non-absorbers) versus X-ray hardness ratio for 67 galaxies in our sample. As X-ray ratio increases, the fractional proportion of H I absorbers (red circles) also increases (shown as text labels for each grey-shaded order-of-magnitude bin in X-ray ratio) relative to the number of non-absorbers (blue triangles). We also plot the trends for the detections (red dashed line) and the whole sample including upper limits as determined by survival analysis (blue solid line), confirming a trend at 4.71σ in optical depth versus X-ray hardness ratio.

the complete sample (excluding our BETA sample), with the same increase in fraction as X-ray ratio increases.

Overall, based on this sample of 20 H I absorbers and 74 non-absorbers, we find that the X-ray hardness ratio $\frac{f_5}{f_1}$ derived from *XMM–Newton* presents a useful diagnostic for increasing the chance of an H I absorption detection. We also find in this limited sample evidence for a positive correlation between optical depth and X-ray ratio at a significance of 3.04σ for the detections and 4.71σ including upper limits, affirming the notion that these different probes of hydrogen near an AGN are tracing similar, if not the same, spatial regions of gas. With a larger sample of H I absorbers and non-absorbers, such as we expect to obtain with the upcoming FLASH search towards 150 000 background galaxies or via other large-scale H I absorption line surveys, we can confirm this trend with even higher statistical significance.
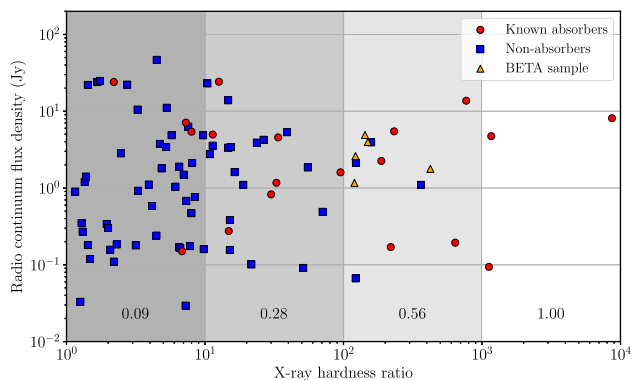
Figure 5. Radio continuum flux versus X-ray hardness ratio for both the sample of 94 galaxies (shown as red circles for H I absorbers and blue squares for non-absorbers) and for our BETA sample (orange triangles). We chose our BETA sample to occupy the high end of X-ray ratio parameter space (where the fraction of absorbers is high) and to be brighter than 1 Jy in radio emission.

2.2 Manual reprocessing of X-ray data

Our analysis above was based on using the flux values as reported in the 3XMM-DR4 catalogue, which are measured by running a standard pipeline on all serendipitously detected sources in a given *XMM–Newton* observed field. The subtleties of reducing data for individual but varied sources and potential impact on the resulting flux values means that we must gauge the reliability of the pipeline-produced catalogue versus the manually intensive but more accurate procedure of reducing each observation by hand. As such, we tested the accuracy of the flux values of the 3XMM-DR4 catalogue by manually reprocessing *XMM–Newton* data from a selection of sources from Table 1. All 20 H I absorbers were selected, while a random selection of 11 non-H I absorbers across a range in flux was used. Fewer non-H I absorbers were investigated as they were found to be more consistent with the catalogue data.

XMM–Newton data were downloaded from NASA's High Energy Astrophysics Science Archive Research Centre (HEASARC) archive. For each source, we selected the single longest publicly available European Photon Imaging Camera (EPIC) observation and re-processed the data using standard tasks from the Science Analysis System (SAS) version 14.0.0 software tool. First, we excluded high particle background exposure time intervals. We used the standard flagging criterion FLAG=0, along with #XMMEA_EM and #XMMEA_EP for the MOS and pn detectors, respectively. Patterns 0–12 were used for MOS and 0–4 for pn. Background-subtracted spectra were extracted using source regions of 35 arcsec radius (for crowded fields, smaller regions were used) and local background regions at least three times larger and of similar distance from the readout nodes. We used the SAS task *epatplot* to identify any sources significantly affected by pileup. Three sources that were badly affected by pileup were excluded from the comparison sample as they would have been subject to increased uncertainties. Individual spectra for MOS1, MOS2 and pn were extracted and then combined using *epicspeccombine* to create a weighted-average EPIC spectrum. This spectrum was then grouped to at least 20 counts per bin in order to use χ^2 statistics. We used XSPEC version 12.8.2 (Arnaud 1996) for all spectral analysis.

Each source was initially fitted with a *phabs* × *zphabs* × *pexriv* (Magdziarz & Zdziarski 1995) model, describing non-intrinsic photoelectric absorption, photoelectric absorption at the redshift of the
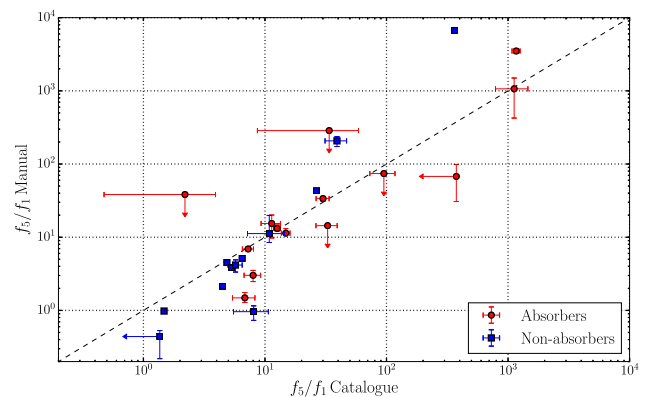
Figure 6. Comparison of flux ratios (f_5/f_1) between catalogue-derived values and manually extracted values. Red circles represent H I absorbing sources while blue squares represent non-absorbing sources. Arrows indicate upper limits. The black dotted line represents catalogue-listed fluxes equal to fitted fluxes. Ignoring upper limits, we find a Spearman rank of $r = 0.86 \pm 0.04$.

galaxy and a power-law reflection component. Here, the *phabs* component is fixed to the line-of-sight absorption contribution while the *zphabs* component is left free (with redshift fixed to its respective host redshift). For most of the non-absorbers, this model is sufficient to replicate the continuum. For some of the absorbers, additional components, such as *mekal* (hot diffuse gas) and *reflect* (reflection from neutral material) components, were required to obtain good fits. Using the *cflux* component, the fluxes in bands 1 (0.2–0.5 keV) and 5 (4.0–12.0 keV) were determined. Finally a ratio of these two fluxes was calculated and compared with the catalogue equivalent for each of our selected sources (Fig. 6). Removing upper limits, we find a strong correlation between the manually extracted and catalogue flux values (Spearman rank $r = 0.86 \pm 0.04$ using a Monte Carlo perturbation error analysis).

Five significant outliers were ignored for this analysis. One of these, H I absorber J125711−172434, has a hardness ratio from the catalogue of ∼1 which upon inspection of the data is due to its location at the centre of a dense cluster (Abell 1644). The galaxy is embedded in very hot 'sloshing' cluster gas at a luminosity of ∼10^{42} erg s^{-1} (Johnson et al. 2010), likely to be dwarfing emission from the AGN and thus responsible for its observed flat spectrum. Due to the complicated nature of this particular system and difficulty in extracting meaningful information from the spectral data, we excluded it from this analysis. The other four outliers were all highly absorbed, and likely Compton-thick, sources ($N_H > 10^{24}$ cm^{-2}). In the catalogue, the flux in the soft band for those sources is extremely low ($f_1 \ll f_5$) but non-negligible. However, our individual modelling of the higher energy continuum suggests that the direct flux from the AGN should be completely absorbed (below the detection limit) in the softest band. Thus, the residual emission detected in that band must have a different origin: either from the host galaxy (at much lower N_H) or from the AGN, but scattered into our line of sight above the obscuring material. In any case, the catalogue value of the hardness ratio $\frac{f_5}{f_1}$ will be an underestimate of the true hardness ratio for the direct AGN emission component. Although this only occurs in a small number of sources, and seems to be restricted to H I absorbing sources, we still advise caution when using the X-ray flux ratios to estimate H I absorption, specifically for strong absorbers. Future methods that we adopt for selecting X-ray absorbed sources will be developed on the basis of the caveats revealed by our analysis here, however we conclude that the simple measure of X-ray

Table 2. Properties of our complete X-ray sample. A total of 11 southern-sky sources were identified on the basis of radio brightness (> 1 Jy), X-ray hardness (> 100), declination $\delta < 0°$ and Galactic latitude $|b| \geq 5°$. The radio flux densities were obtained from either NVSS at 1.4 GHz (Condon et al. 1998) or SUMSS (Mauch et al. 2003) at 843 MHz. Of these, three galaxies are known H I absorbers (five including PKS 1740−517 and PKS 1657−298). For observations with BETA, redshifts were either unknown or selected to be in the range $0.4 < z < 1.0$. The sample observed with BETA, including PKS 1740−517, occupies the bottom half of this table. The last column indicates the presence or absence of H I absorption; we note that we can only rule out H I absorption for our BETA sample within our searched redshift range.

Source	XMM name	RA, Dec. J2000	$S_{1.4}$ (Jy)	$S_{0.8}$ (Jy)	X-ray ratio	z	R band (mag)	H I abs.
PKS 0625−545	J062648.7−543208	06:26:49.58, −54:32:34.7[a]	–	1.15	487	0.052[a]	14.5[p]	?
PKS 0859−25	J090147.2−255516	09:01:47.50, −25:55:18.7[b]	6.25	–	481	0.305[i]	18.9[p]	?
NGC 4945	J130527.4−492804	13:05:27.48, −49:28:05.6[c]	–	5.55	3764	0.002[j]	9.5[q]	Y
PKS 1549−79	J155658.9−791403	15:56:58.87, −79:14:04.3[d]	–	6.19	1167	0.152[k]	17.9[p]	Y
PKS 1814−63	J181935.0−634547	18:19:35.00, −63:45:48.2[d]	–	19.89	770	0.063[m]	15.6[p]	Y
PKS 1547−79	J155521.7−794036	15:55:21.65, −79:40:36.3[e]	–	6.01	143	0.483[n]	19.1[p]	N
PKS 1657−298	J170109.8−295439	17:01:09.71, −29:54:41.8[b]	1.78	–	424	0.420[r]	–	Y
MRC 1722−644	J172657.7−642751	17:26:57.85, −64:27:53.4[f]	–	4.14	150	–	–	N
PKS 1740−517	J174425.3−514444	17:44:25.45, −51:44:43.8[d]	–	8.15	8689	0.441[l]	20.8[n]	Y
PKS 2008−068	J201114.2−064403	20:11:14.23, −06:44:03.4[g]	2.60	–	122	0.547[o]	*21.2[o]	N
PKS 2154−11	J215644.1−112747	21:56:44.10, −11:27:49.5[h]	1.16	–	120	–	–	N

[a]Cava et al. (2009) [b]Douglas et al. (1996) [c]Greenhill, Moran & Herrnstein (1997) [d]Johnston et al. (1995) [e]di Serego-Alighieri et al. (1994) [f]Murphy et al. (2010) [g]Mahony et al. (2011) [h]Condon et al. (1998) [i]Burgess & Hunstead (2006) [j]Koribalski et al. (2004) [k]Holt, Tadhunter & Morganti (2008) [l]Allison et al. (2015) [m]Ramos Almeida et al. (2011) [n]Tadhunter et al. (1993) [o]Snellen et al. (2002) [p]Hambly et al. (2001) [q]Doyle et al. (2005) [r]this work
*Observed with *r*-band filter at 6814 Å by Snellen et al. (2002)

hardness ratio $\frac{f_S}{f_1}$ is a useful method to first order to select for likely H I absorbers.

3 ASKAP–BETA TEST OBSERVATIONS OF X-RAY ABSORBERS

In order to test correlation between soft X-ray absorption and H I absorption, we compiled a list of candidates to be potentially observed with BETA. We began with a broader set of criteria defining a set of southern-sky sources, which we then narrowed to meet further redshift requirements specific to BETA. Our initial broad criteria were:

(1) Radio flux $S > 1$ Jy (in SUMSS or NVSS)
(2) X-ray hardness ratio $\frac{f_S}{f_1} > 100$ in 3XMM-DR4
(3) Declination $\delta < 0°$
(4) Galactic latitude $|b| \geq 5°$

The adoption of these first criteria was primarily driven by the sensitivity limitations of BETA in its 6-antenna configuration. This made it necessary to target the brightest radio sources ($S > 1$ Jy) in order to reach a reasonable optical depth sensitivity within an initial 3 hr observation. Because there were no candidates that were both brighter than 1 Jy in radio and with X-ray ratios > 1000 that were not already known H I absorption detections, we lowered the X-ray ratio threshold to investigate whether ratios > 100 still predicted H I absorption in the same way as the most-absorbed X-ray spectra, with the expectation that we were less likely to detect H I absorption in this parameter space than those sources with higher ratios. We note that applying these criteria results in a total of 11 candidate sources (seven from SUMSS, four from NVSS). However, of these, four sources are known H I absorbers (NGC 4945, PKS 1549−79, PKS 1740−517, PKS 1814−63) while an additional two sources are beyond the redshift range we targeted with BETA (PKS 0625−545 at $z = 0.05$ and PKS 0859−25 at $z = 0.3$). None the less, this full sample provides a useful parent set based on clear criteria from which we draw our BETA subset. An overview of the properties of the entire sample is given in Table 2 along with the respective

references. The top half of Table 2 contains sources with $z < 0.4$, of which the three galaxies with the highest X-ray hardness ratios already have known detections of H I absorption while the other two have yet to be searched. The bottom half of Table 2 contains our BETA sample detailed in this paper, as well as PKS 1740−517 described in Allison et al. (2015); in the same way, the two sources with the highest X-ray hardness ratios also feature H I absorption, which is consistent with our findings in Section 2. Each source is detected in the mid-infrared, and so we include their positions overplotted on the Wright et al. (2010) WISE colour–colour plot in Fig. 7 to give insight into the likely properties of their host galaxies. From this, we see that this sample spans a range in galaxy types based on WISE colours, although mostly occupying the region near the QSO class.

The final list of candidates observed with ASKAP–BETA (the bottom half of Table 2) were required to meet the following additional criterion:

(5) (if known) redshift z in the range $0.4 \leq z \leq 1.0$.

For our observed sample we focused on the redshift range $0.4 \leq z \leq 1.0$ as this corresponds to Band 1 of BETA (711.5–1015.5 MHz), which was the band primarily used during commissioning, allows access to the most redshift parameter space at once, is the least affected by RFI and is the most unexplored in terms of H I absorption. This leaves our BETA X-ray pilot sample at a total of five sources (six including PKS 1740−517), described in more detail in the next section. We do not discuss the properties of PKS 1740−517 here and instead refer the reader to Allison et al. (2015) for details about this source.

3.1 Properties of our observed sample

Here we summarize what has been previously reported about each source in our pilot sample. We show the radio spectral energy distribution for each source in Fig. 8 to give an insight into their radio continuum properties, with detail given in Section 3.2. We searched for potential optical counterparts in the NASA/IPAC Extragalactic
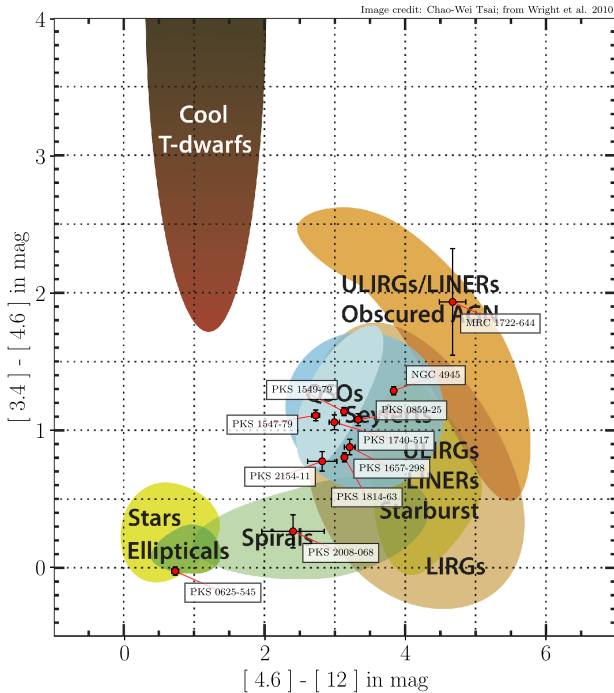
Figure 7. The 11 radio sources in our total sample (including the 5 sources presented in this paper) plotted on the Wright et al. ([2010](#)) WISE colour–colour diagram to give an insight into the properties of their likely host galaxies. Our sources occupy a range in possible galaxy type, including elliptical, spiral, Seyfert, QSO and ULIRG.

Database (NED) and SuperCOSMOS blue/red surveys (within 5 arcsec). We also checked to see if the sources have been observed at high angular resolution in radio, using very long baseline interferometry (VLBI).

3.1.1 PKS 1547−79

A source known to be linearly polarized at a level > 5 per cent across the range from 10–30 cm wavelengths (Gardner & Davies [1966](#)), it was also included in the Kuehr et al. ([1981](#)) sample based on its 5 GHz flux density being > 1 Jy. It was imaged at 2 arcsec resolution by Duncan & Sproats ([1992](#)) revealing a double-lobed structure and central radio source. It is part of the 2 Jy sample of Tadhunter et al. ([1993](#)) who confirmed an optical redshift of $z = 0.483$, and has been identified as a broad line radio galaxy (BLRG) likely interacting with nearby companions. PKS 1547−79 was also part of an *XMM–Newton* study conducted by Mingo et al. ([2014](#)), who found a high intrinsic N_H from X-ray absorption of $\sim 9.9 \times 10^{23}$ cm^{-2} potentially indicating a Compton-thick medium surrounding the AGN.

3.1.2 PKS 1657−298

This is a largely unknown and unstudied radio galaxy, identified as a compact double at VLBI resolution. Due to its low Galactic latitude ($+7°$), there has been no optical counterpart identified and no previously known redshift for the galaxy. During a study of *ROSAT* X-ray sources in globular clusters, Verbunt ([2001](#)) identified the X-ray counterpart for this galaxy within the field of view to a positional accuracy of 3 arcsec. Petrov, Honma & Shibata ([2012](#)) provide the most accurate position for this source based on VLBI data at 22 GHz.

3.1.3 MRC 1722−644

First identified in MRC at 408 MHz as 1722−644, this is a radio source of mostly unknown multi-wavelength properties. It is a compact double at VLBI resolution (Edwards & Tingay [2016](#)), and has no known redshift or optical counterpart. This source is part of the GPS class of radio sources, due to its spectral peak at 1 GHz, and features a very narrow radio spectrum (Edwards & Tingay [2004](#)).

3.1.4 PKS 2008−068

One of the more well-studied sources in our sample, this galaxy falls into the category of GPS sources with its peak at 1.6 GHz. Similar to our other sources, it is compact on VLBI scales. It is known to be a weakly-polarized source (Berge & Seielstad [1972](#)), at a level of 1 per cent at 10 GHz (Inoue et al. [1995](#)). It has a confirmed optical redshift $z = 0.547$ (Snellen et al. [2002](#)).

3.1.5 PKS 2154−11

A mostly obscure radio source with little known about the properties of the host galaxy. It has been detected across the radio spectrum from 80 MHz to 20 GHz and was reported as extended at 20 GHz (Murphy et al. [2010](#)). Its WISE colours place it in the QSO class of Fig. 7, but there is no known optical counterpart and no reported redshift.

3.2 Spectral modelling at low radio frequencies

The sources in which we searched for H I absorption with BETA were also observed as part of the low radio frequency all-sky survey conducted by the Murchison Widefield Array (MWA, Tingay et al. [2013](#)). The GaLactic and Extragalactic All-sky MWA survey (GLEAM, Wayth et al. [2015](#); Hurley-Walker et al. [2017](#)) observed the entire sky south of $+30°$ declination at twenty different frequencies between 72 and 231 MHz. The extragalactic catalogue formed from the GLEAM survey consists of 307 455 sources, with positions accurate to ~ 30 arcsec. This low radio frequency data allows us to constrain the spectral shape of the sources and, in cases where free–free absorption is responsible for a spectral turnover, infer the density of the ionized medium in a source (e.g. Callingham et al. [2015](#)).

We fit the following generic curved model to characterize the radio spectrum of the five sources searched for H I absorption with BETA:

$$S_\nu = \frac{S_p}{(1 - e^{-1})} \left[1 - e^{-(\nu/\nu_p)^{\alpha_{thin} - \alpha_{thick}}} \right] \left(\frac{\nu}{\nu_p} \right)^{\alpha_{thick}}, \qquad (1)$$

where α_{thick} and α_{thin} are the spectral indices in the optically thick and optically thin regimes of the spectrum, respectively. S_p is the flux density at the peak frequency ν_p (Snellen et al. [1998](#)). The standard non-thermal synchrotron power-law of the form

$$S_\nu = a\nu^\alpha, \qquad (2)$$

where a characterises the amplitude of the synchrotron spectrum, was also fit to the spectrum if the source did not display significant spectral curvature. The procedure implemented here to fit the spectra is identical to that outlined in Callingham et al. ([2016](#)). In summary, a Markov Chain Monte Carlo algorithm was used to sample the posterior probability density functions of the various model parameters such that the applied Gaussian likelihood function was maximized under physically sensible uniform priors. The simplex

Table 3. The best-fitting statistics of the generic curved model from equation (1) for PKS 1547−79, PKS 1657−298, MRC 1722−644 and PKS 2008−068. Only the parameters from the non-thermal power-law fit are presented for PKS 2154−11 since it is best fit by that model. Note that the curvature evident in the spectrum of PKS 1547−79 is most likely the product of a spectral break occurring near 1.4 GHz or the spectrum becoming dominated by core emission, rather than an absorption process.

Name	S_p (Jy)	ν_p (MHz)	α_{thick}	α_{thin}	a (Jy)
PKS 1547−79	4.0 ± 0.5	1390 ± 150	-0.4 ± 0.1	-1.4 ± 0.2	−
PKS 1657−298	9.1 ± 0.3	100 ± 30	0.1 ± 0.2	-0.9 ± 0.2	−
MRC 1722−644	4.6 ± 0.1	930 ± 40	1.6 ± 0.1	-1.2 ± 0.1	−
PKS 2008−068	3.0 ± 0.2	740 ± 10	1.7 ± 0.1	-0.8 ± 0.1	−
PKS 2154−11	−	−	−	-1.0 ± 0.1	1.4 ± 0.2

algorithm introduced by Nelder & Mead (1965) was used to direct the walkers to the maximum of the likelihood function.

PKS 1547−79, PKS 1657−298, MRC 1722−644 and PKS 2008−068 all display significant curvature in their spectra between 72 MHz and 20 GHz, and are best fit by equation (1). Only PKS 2154−11 is best fit by the simple power law of equation (2). The best-fitting statistics for the five sources are presented in Table 3 and the data are plotted in Fig. 8. Note that the spectral peak for PKS 1657−298 is only just detected within the GLEAM band, which means the optically thick spectral index for this source has a large uncertainty since the spectrum is not completely sampled below the turnover.

3.3 BETA observations and data reduction

Each source in our sample was observed with BETA for a number of hours during the time available for commissioning observations. An initial 3 hr observation was used to check for obvious absorption signatures. The minimum total integration time was chosen to ensure sensitivity to optical depths $\tau \geq 0.05$, with more time spent integrating on sources where possible. We give details of the observations in Table 4. For one source (PKS 2154−11), we could only reach an optical depth sensitivity of $\tau \geq 0.07$ due to its low flux density and limits in available commissioning time. At certain times only a subset of the 6-antenna BETA was available in which case we made use of all working antennas. The data were reduced following the procedure described by Allison et al. (2015). For an individual source, the final spectrum was produced from the combination of all good data sets available. These spectra are shown in Figs 16 to 20, located at the end of this article. We identified the possible absorption signature in PKS 1657−298 in the first 3 hr observation of the source, and followed it up with several more hours of observation to obtain a higher signal-to-noise spectrum for analysis. We describe its properties in detail in the following section.

4 PKS 1657−298: A NEW H I ABSORBER

From our BETA pilot study, we discovered a new H I absorption line towards PKS 1657−298. Of the five sources observed, this radio source featured the largest X-ray hardness ratio of 424 (whereas the others were closer to ∼100), thus making this detection of H I absorption consistent with our findings in Section 2. As described in Section 3.1, there is very little known about this source in general, most probably due to its inconvenient location at a Galactic position of $l = 353.7°$, $b = 7.4°$, making it an unlikely target for optical and infrared studies. Fig. 9 shows an X-ray image from *Chandra* (obtained from the online archive) of PKS 1657−298 overlaid with radio contours from NVSS at 1.4 GHz. There are several serendipitous observations of this source in both the *Chandra*

and *XMM–Newton* archives due to its spatial location near to the low mass X-ray binary MXB 1659−298.

As stated in Section 3.1, there is no known redshift for PKS 1657−298. Aside from the H I detection at a redshift of $z = 0.42$, we do not currently have other multi-wavelength evidence confirming the same redshift for our assumed host radio galaxy. There is also the possibility that the coincident radio and X-ray sources are not physically associated. To address this, if we consider the number density of X-ray sources in the 3XMM-DR4 release equal to or brighter than the integrated flux of PKS 1657−298 (14 deg^{-2} for fluxes $\geq 7.5 \times 10^{-13}$ erg cm^{-2} s^{-1}) and the number density of radio sources in NVSS similarly equivalent in flux density (0.02 deg^{-2} for flux densities ≥ 1777 mJy), then the Poisson probability of finding a source of each kind within a 30 arcsec radius is 0.000 001 per cent, driven mostly by the radio brightness of PKS 1657−298. If we instead consider that we specifically selected bright radio sources and ask what the chance of any X-ray source nearby is (based on the density of 3XMM-DR4 sources of 469 deg^{-2}), then we find a similarly-low probability of 0.004 per cent. As such, based on this alone we conclude that the radio and X-ray sources are almost certainly physically associated. In order to detect the H I absorption, we know that the redshift of the radio source is definitely $z \geq 0.42$ as it must be acting as a background source. We can thus consider the implications of the well-studied K-z relation for radio/infrared galaxies (Lilly & Longair 1984), which describes the correlation between K-band magnitude (2.17 μm) and redshift z. In particular, we compare the infrared properties of PKS 1657−298 with the results of Willott et al. (2003). Although the galaxy is visible in 2MASS-K, it is not catalogued, possibly due to its proximity to a nearby source of similar brightness (17011004−2954423). We applied basic aperture photometry to estimate the individual brightnesses of each source and we find that they are consistent within errors to each other. Thus, we can adopt the same magnitude for PKS 1657−298, indicating a K-band magnitude of 14.9±0.1 as catalogued in 2MASS. There is a chance that the recorded magnitude is due to the blended combination of each source, in which case the true K-band magnitude would be ∼15.6. However, when applying the same basic aperture photometry to nearby objects of similar counts (namely, 17011007−2955021 and 17011032−2954228), we find similar K-band magnitudes of ∼14.9 which suggests that this is an accurate estimate for PKS 1657−298 also. None the less, we also consider the 'deblended' scenario below.

Assuming the same redshift as derived from the H I absorption, we plot the K-z position of PKS 1657−298 (red circle) in Fig. 10 alongside the other data sets as studied in Willott et al. (2003). Assuming the 2MASS-K magnitude is blended with the nearby source, we additionally plot the deblended magnitude for PKS 1657−298 (orange star) for comparison. We also plot the best fit reported in Willott et al. (2003) as a solid line. Based on the K-z relation data, we
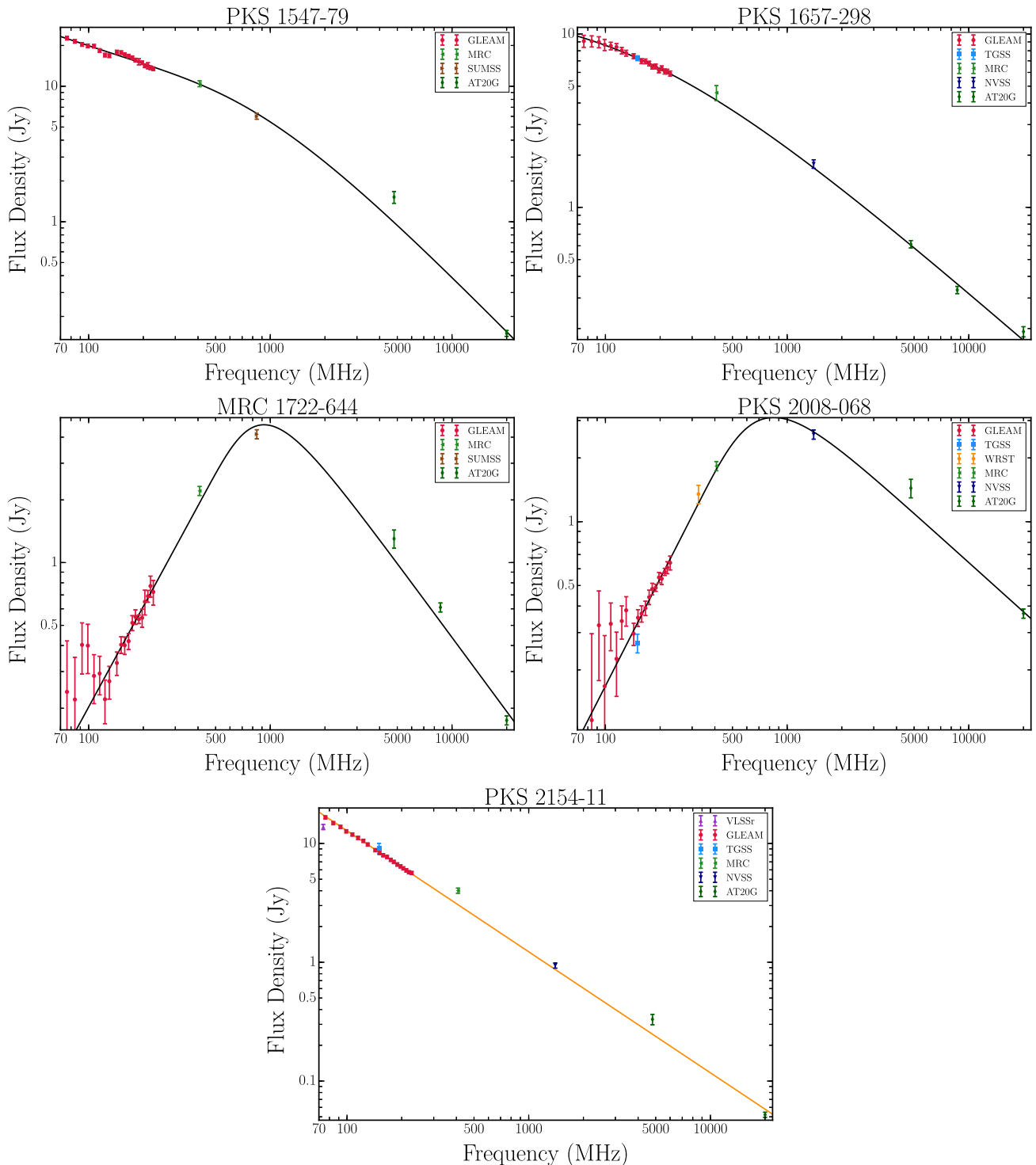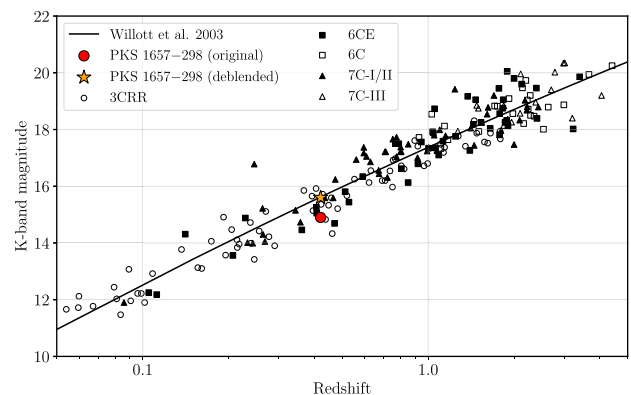
Figure 8. Radio spectral energy distributions for the BETA sample. The black curve represents the fit of equation (1) to all of the available data. PKS 2154−11 shows no evidence of curvature in its spectrum, and thus is fit with a standard power-law fit, as shown by the orange line. The surveys appearing here include (ordered from lowest to highest frequency): the Very Large Array Low-Frequency Sky Survey redux at 75 MHz (VLSSr, Lane et al. 2014), the GaLactic and Extragalactic All-sky MWA survey at 72–231 MHz (GLEAM, Wayth et al. 2015; Hurley-Walker et al. 2017), the TIFR GMRT Sky Survey ADR1 at 150 MHz (TGSS-ADR1, Intema et al. 2017), a sample of GPS sources observed with the Westerbork Synthesis Radio Telescope at 327 MHz (WSRT, Stanghellini et al. 1998), the Molonglo Reference Catalogue at 408 MHz (MRC, Large et al. 1981), the Sydney University Molonglo Sky Survey at 843 MHz (SUMSS, Mauch et al. 2003), the NRAO VLA Sky Survey at 1.4 GHz (NVSS, Condon et al. 1998) and the Australia Telescope 20 GHz survey (AT20G, Murphy et al. 2010).

Table 4. Table containing details of the observations of each galaxy in our BETA sample. We record here the date of the observation, the total hours spent integrating on source, the antennas included in the array, the resulting RMS noise per channel and corresponding 5σ optical depth sensitivity.

Source	Date	t_{int} (hr)	Antenna numbers	σ_{chan} (mJy beam^{-1})	$5\sigma_\tau$
PKS 1547−79	2014 November 14	3	1, 3, 6, 8, 9, 15	29	0.024
	2016 January 29	5	1, 3, 8, 15	35	0.029
	Total	8	–	23	0.019
PKS 1657−298	2014 November 21	3	1, 3, 6, 8, 9, 15	29	0.058
	2015 May 15	3.25	1, 3, 6, 8, 9, 15	28	0.056
	2015 June 9	10	1, 3, 6, 8, 15	19	0.038
	2015 August 24	6	1, 3, 6, 8, 15	25	0.050
	2015 October 2	5	1, 3, 6, 8, 15	27	0.054
	Total	27.25	–	11	0.022
MRC 1722−644	2014 November 15	3	1, 3, 6, 8, 9, 15	29	0.032
	Total	3	–	29	0.032
PKS 2008−068	2014 November 22	2	1, 3, 6, 8, 9, 15	35	0.058
	2014 November 23	2	1, 3, 6, 8, 9, 15	35	0.058
	2015 June 9	3	1, 3, 6, 8, 15	35	0.058
	2015 October 5	5	1, 3, 6, 8, 15	27	0.045
	2016 January 30	1.5	1, 3, 8, 15	64	0.107
	2016 February 1	2	1, 3, 8, 15	55	0.092
	Total	15.5	–	17	0.028
PKS 2154−11	2015 May 7	3	1, 3, 6, 8, 9, 15	29	0.097
	2015 October 22	3.1	1, 3, 6, 8, 15	35	0.117
	2016 January 27	1.2	1, 3, 8, 15	72	0.240
	2016 January 27	0.9	1, 3, 8, 15	83	0.277
	2016 January 27	2	1, 3, 8, 15	55	0.183
	2016 January 31	3	1, 3, 8, 15	45	0.150
	Total	13.2	–	22	0.070
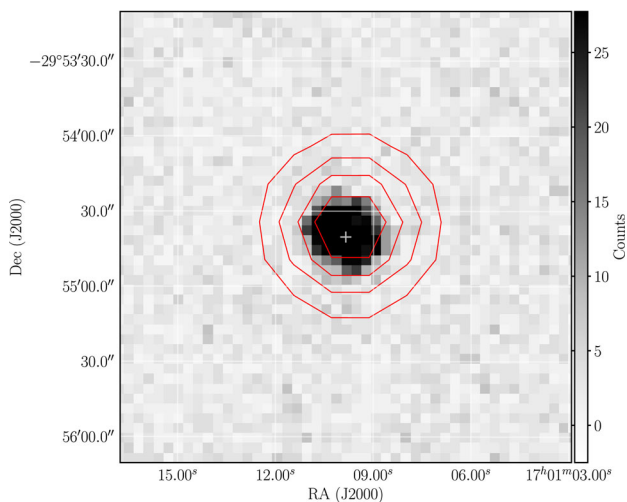
Figure 9. X-ray image of PKS 1657−298 from *Chandra* data (obtained via the *Chandra* Search and retrieval service for observation ID 13711), overlaid with radio contours from NVSS at 1.4 GHz (shown in red). The contours range from 20 per cent to 80 per cent of the peak in four equally spaced levels.

Figure 10. Scatter plot of *K-z* relation data from Willott et al. (2003), including their best-fitting line to the data. We have plotted the position of PKS 1657−298 as a red circle, based on its redshift assumed from the H I absorption data and *K*-band magnitude from 2MASS. The deblended magnitude assuming blending with 17 011 004−2954 423 is shown as an orange star. We see that this is in good agreement with the *K-z* relation, and in fact the assumption of a higher redshift for the galaxy is less consistent with existing data.

see that a redshift of $z = 0.42$ is very much consistent with the 2 µm properties of PKS 1657−298 (either catalogued or deblended) and that a higher redshift (that is, a more distant radio galaxy) is actually less consistent with the relation. We note that reddening due to Galactic extinction (~ 0.1 mag at 2 µm) has very little impact on this result and is well within the scatter, and further that, if not blended

with 17011004−2954423, PKS 1657−298 is slightly brighter than we might expect based on the *K-z* relation which may indicate an unusually luminous host. Based on this result, we conclude that the H I absorption detected towards PKS 1657−298 is likely to be located at the same redshift as the coincident radio/X-ray sources.

We conducted a multi-wavelength search in order to characterize the properties of this source as best as possible based on existing
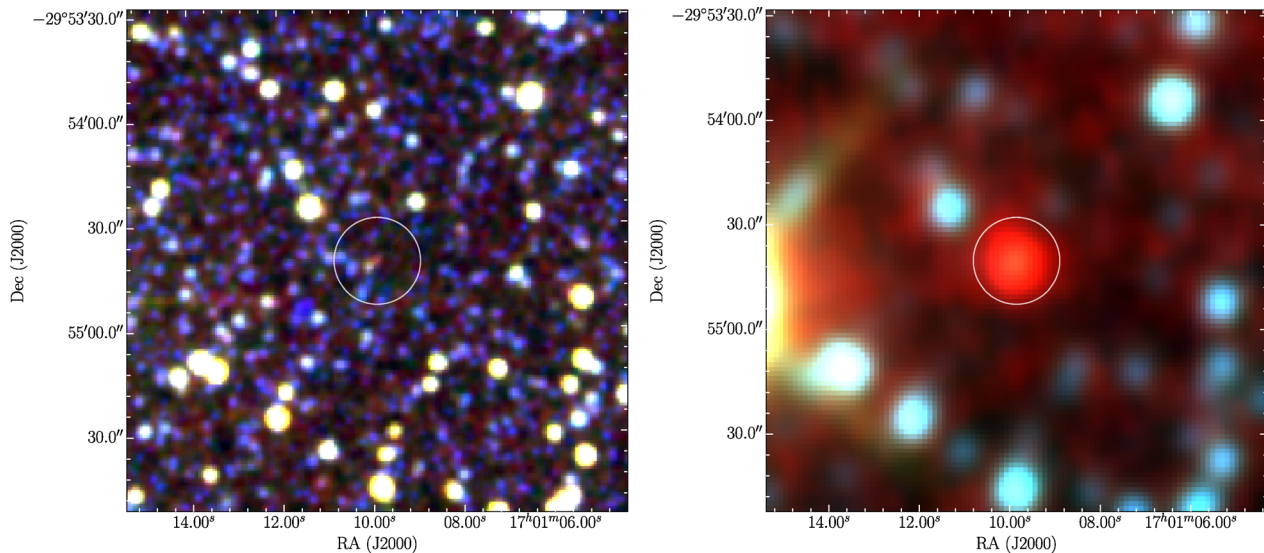
Figure 11. Three-colour optical/infrared images of PKS 1657−298. Left-hand panel: image formed from 2MASS-K (red), 2MASS-J (green) and UKST-B (blue) with each image scaled to 95 per cent percentile. A small red blob is seen at 2 μm, with non-detections in the other bands. Right-hand panel: image formed from WISE 12 μm (red), 4 μm (green) and 3 μm (blue) also scaled to their 95th percentiles. The galaxy is detected clearly in each band but is brightest at 12 μm. In both cases, the white circles are centred on the VLBI position measured by Petrov et al. (2012).

data. Fig. 11 shows three-colour images of PKS 1657−298 using available optical/infrared data from DSS/DSS2 (Lasker et al. 1990; McLean et al. 2000), SuperCOSMOS (Hambly et al. 2001), 2MASS (Skrutskie et al. 2006) and WISE (Wright et al. 2010). The left-hand panel is formed from 2MASS-K (red), 2MASS-J (green) and UKST-B (blue) with each image scaled to 95 per cent percentile. There is a small source evident in the 2MASS-K image at 2 μm, although it is absent from the other two bands and also not detected in 2MASS-J or 2MASS-H. This absence of detection cannot be solely attributed to Galactic extinction, given that 2MASS-J and 2MASS-H are more sensitive than 2MASS-K and that it is very tentatively visible in ESO-R (implying an *R*-band magnitude $\gtrsim 21$ mag). Instead, the lack of clear detection at optical/infrared wavelengths (with the exception of the *K* band) implies a high level of intrinsic reddening due to dust and gas. This is consistent with the recent findings of Curran et al. (2017), specifically that the detection rate of H I absorption increases towards 100 per cent as the *B–K* colour increases. The right-hand panel of Fig. 11 shows a three-colour image formed from WISE 12 μm (red), 4 μm (green) and 3 μm (blue) also scaled to their 95th percentiles in intensity. PKS 1657−298 is detected significantly in all WISE bands, however it has a considerable excess in emission at 12 μm causing the evident reddening in the image. This is consistent with the conclusion based on DSS/SuperCOSMOS/2MASS that it is intrinsically (strongly) reddened. The overlaid white circles in each panel are centred on the VLBI position for PKS 1657−298 from Petrov et al. (2012). As seen in Fig. 7, PKS 1657−298 occupies a region of the diagram shared by Seyferts and LIRGs which gives us the current best insight into the properties of the host without better optical data.

The VLBI data currently available for PKS 1657−298 are limited, however do provide further insight into the properties of the host. From previous observations of the source at 2.3 GHz and 8.4 GHz (accessed via http://astrogeo.org), we can estimate the diameter of the radio source (apparently split into two compact components) to be between ∼10–15 mas. At a redshift of $z = 0.42$, this corre-

sponds to a physical extent of ∼50–80 pc which is consistent with a typical compact symmetric object (CSO). Based on the limited U-V coverage and sensitivity of these current data, we do not have information about whether we are seeing two jet components or a core/jet system, nor can we determine the relative flux density of each component.

4.1 H I absorption properties

We describe here our analysis of the H I absorption towards PKS 1657−298 as detected with BETA. We model the absorption line as a superposition of Gaussian profiles and then determine the best-fitting number of components and marginal distributions for the line parameters using a Bayesian approach as described by Allison et al. (2015, 2017) and references therein. We identify a single component in the absorption-line profile of PKS 1657−298, at a redshift of $z = 0.420164 \pm 0.000006$. We show the marginal posteriors for key parameters in Fig. 13. The peak and integrated optical depths of the line are 0.046 ± 0.002 and $\int \tau \mathrm{d}v \, \mathrm{km \, s^{-1}} = 2.9 \pm 0.1$, respectively. Dividing these two values we obtain an effective line-width of $63^{+4}_{-3} \, \mathrm{km \, s^{-1}}$. Assuming a spin temperature of 100 K and a covering factor of 1 (to maintain consistency with previous work), we obtain a column density of $N_{\mathrm{HI}} = 5.3 \pm 0.3 \times 10^{20} \, \mathrm{cm^{-2}}$.

These properties are consistent with those typically measured for H I absorption associated with radio AGN (e.g. Gereb et al. 2015). The symmetry and width of the line are consistent with the compact radio source illuminating a regular gaseous structure (such as a disc) near to the systemic velocity of the host galaxy. There is some hint at low significance of structure in the main line (potentially two components instead of one) as well as a possible extension bluewards of the main line as seen in Fig. 12. This may be evidence of individual dense clouds or broad outflows. However, as these are below statistical significance in our current data, we defer further speculation to future radio observations of PKS 1657−298. Of key interest from this point is comparing our properties as measured
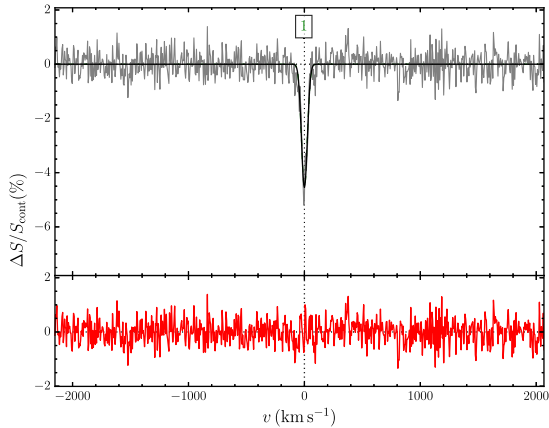
Figure 12. The best-fitting model (black) for our average PKS 1657−298 spectrum (grey). The residual spectrum is shown in red. Details of our method are given in Section 4.1.
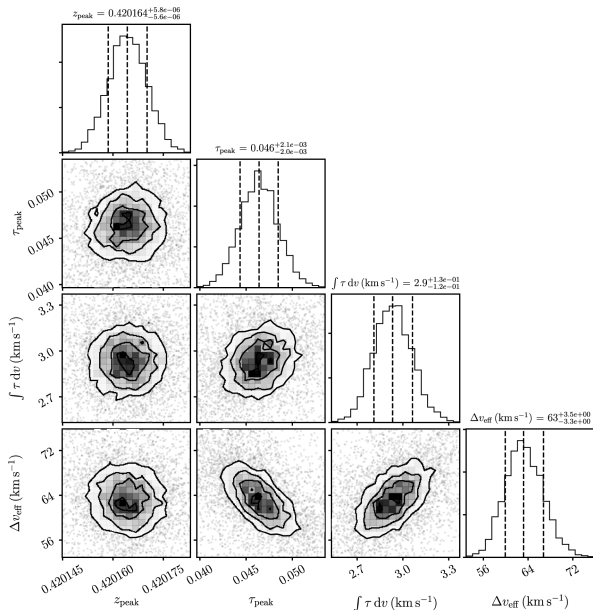

Figure 13. Marginal posteriors for the properties of H I absorption towards PKS 1657−298. From these, we measure the redshift z_{peak}, peak optical depth τ_{peak}, integrated optical depth $\int \tau \, dv$ (km s^{-1}) and effective line-width Δv_{eff} (km s^{-1}).

from the H I absorption with those indicated by the X-ray data available to us for this galaxy.

4.2 X-ray properties: *Chandra*

Chandra observations including PKS 1657−298 in the field of view (observation IDs 5469, 6337, 13711 and 14453) were combined into a single spectrum. The stacked spectrum was then fitted with a simple absorbed power-law model (*tbgrain* × *ztbabs* × *powerlaw*). We adopted these models instead of the standard *phabs* and *zphabs* as they feature more precise elemental cross-sections and allow us to incorporate the presence of line-of-sight molecular hydrogen, which is important at such low Galactic latitudes. In this model, *tbgrain* accounts for the line-of-sight absorption and *ztbabs* for the intrinsic absorption at the redshift of the source (see Wilms, Allen & Mccray 2000 for details of the photo-ionization cross-sections
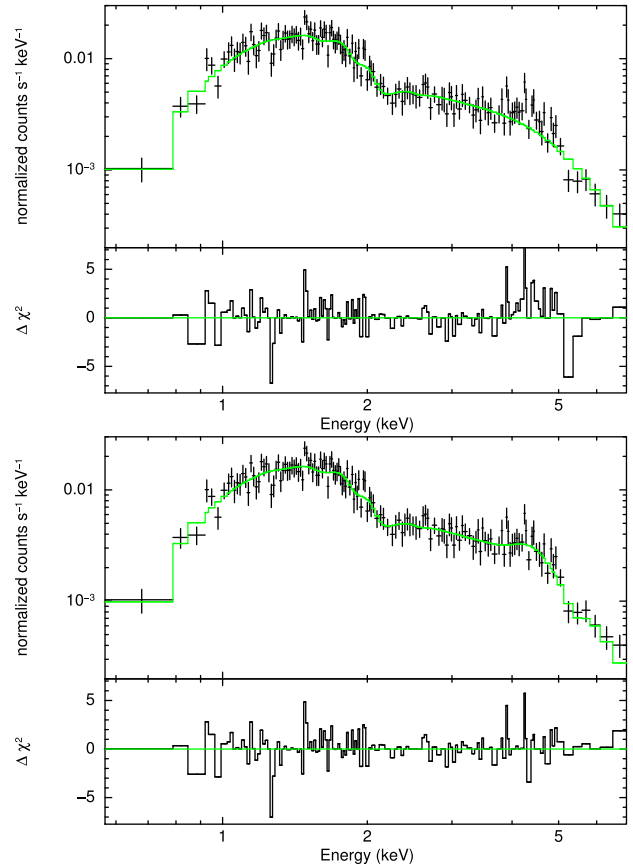
Figure 14. Top: Stacked *Chandra* spectrum for PKS 1657−298 with model fits and residuals. A simple absorbed power-law is used (*tbgrain* × *ztbabs* × *powerlaw*). This results in significant high-energy residuals. Bottom: As in above but we introduce two Gaussian components (one with a negative normalization) to account for the residuals (*tbgrain* × *ztbabs* × (*gauss* + *gauss* + *powerlaw*)). Both spectra have been rebinned to a signal-to-noise of at least 4 for clarity.

in the Tuebingen–Boulder interstellar medium absorption models). We adopted a value of $N_{H, Gal} = 3.1 \times 10^{21}$ cm^{-2} for the line-of-sight component, which is the sum of $N_{HI, Gal} = 1.8 \times 10^{21}$ cm^{-2} and $N_{H2, Gal} = 1.3 \times 10^{21}$ cm^{-2} using the method of Willingale et al. (2013). This was used as an input parameter to *tbgrain* (with default values for the grain phase), where we find that the total column is not very sensitive to changes to the molecular hydrogen fraction. The power-law index returned from this model was $\Gamma = 1.84 \pm 0.10$. This corresponded to a decent ($\chi_\nu^2 \approx 1.12$) fit, however with high-energy residuals present (Fig. 14, top).

We added two Gaussian components to our spectral model: one to simulate an emission line and the other (with a negative normalization) an absorption edge (Fig. 14, bottom). Here, the power-law index of the continuum is found to be $\Gamma = 1.93 \pm 0.15$. We varied the emission line energy between 4 and 6 keV, finding a best fit of $E_{em} = 4.37^{+0.18}_{-0.17}$ keV and equivalent width of $\sigma_{em} = 0.33^{+0.23}_{-0.16}$ keV. At those energies, the intrinsic energy resolution [observed full width at half-maximum (FWHM) of a narrow line] of the ACIS-S3 chip[1] is ∼0.16 keV. The absorption edge energy was tested from 4.5 to 6.5 keV, with a best fit of $E_{abs} = 5.4 \pm 0.4$ keV. This improved the fit to $\chi_\nu^2 \sim 1.02$, with an F-test significance of 99.9 per cent.

---

[1] http://cxc.cfa.harvard.edu/proposer/POG/html/
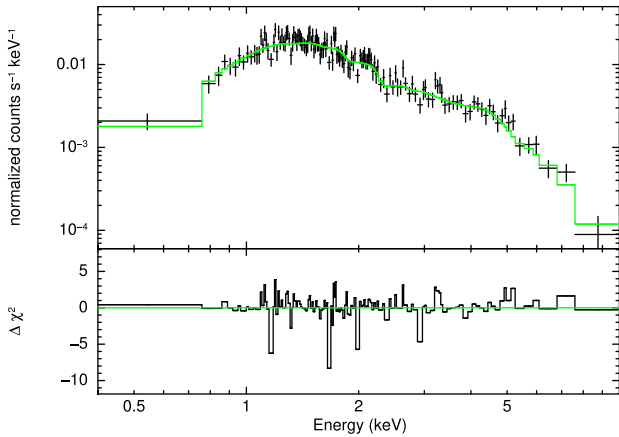
Figure 15. As in Fig. 14 but for the stacked *XMM–Newton* spectrum. Once again, the spectrum has been rebinned to a minimum signal-to-noise of 4.

The emission line can best be interpreted as a narrow Fe line at ~ 6.4 keV in the rest frame of PKS 1657−298; however, we cannot rule that we are instead looking at a broader Fe line at ~ 6.7 keV. The absorption line is consistent with an Fe K-shell absorption edge at a rest-frame energy of 7.1 keV, which is expected from Fe in the same low-ionization states that produce the 6.4 keV emission line. Therefore, the observed energies of these features indicate a redshift of ~ 0.42, consistent with the redshift estimated from the H I data. Alternatively, we cannot rule out the possibility that both the emission line and absorption edge could be replaced by a P-Cygni profile. This scenario corresponds to a strong outflow as seen in high Eddington-ratio quasars such as PDS 456 (Nardini et al. 2015) and PG1211+143 (Pounds & Reeves 2009). Based on these *Chandra* data, we find an observed 0.3–10.0 keV flux $f_x = 4.9^{+0.3}_{-0.3} \times 10^{-13}$ erg cm^{-2} s^{-1} in the observer's frame, and we infer an unabsorbed 0.3–10.0 keV rest frame luminosity (at $z = 0.42$) of $L_x = 5.2^{+0.4}_{-0.3} \times 10^{44}$ erg s^{-1}. We derive a total hydrogen column towards PKS 1657−298 of $N_{H, tot} = 0.9^{+0.2}_{-0.2} \times 10^{22}$ cm^{-2}, of which we estimate that $N_{H,X} = 0.6^{+0.2}_{-0.2} \times 10^{22}$ cm^{-2} is intrinsic to the emitting source.

4.3 X-ray properties: *XMM–Newton*

We also used archival *XMM–Newton* data of PKS 1657−298. We combined the EPIC pn and MOS spectra (and associated response files) from observations 0153190101 and 0205580201 and the EPIC MOS spectra from observations 0008620701 and 0748391601 (the EPIC pn spectra were not available for these observations) into a single stacked spectrum in order to increase the signal to noise. As we did for the combined *Chandra* spectrum, we initially fitted the source with a simple absorbed power law. This resulted in an acceptable fit ($\chi^2_\nu \approx 1.09$). Unlike with *Chandra*, the signal to noise in the stacked spectrum is not high enough to significantly identify residual components, and the addition of a narrow emission line and an absorption edge, or of an emission plus absorption line (to match the *Chandra* spectrum) does not improve the fit statistics ($\chi^2_\nu \approx 1.09$). The 90 per cent-confidence-level upper limit of the normalization of a possible narrow emission line is $K \approx 6.7 \times 10^{-6}$. This is consistent with the equivalent width of the line detected in the *Chandra* spectrum. The continuum plus emission and absorption line model can be seen in Fig. 15 . The power-law index derived is $\Gamma = 1.89 \pm 0.14$, consistent with the *Chandra* spectrum, as is the observed 0.3–10.0 keV flux and unabsorbed rest frame luminosity;

$f_x = 4.8^{+0.3}_{-0.3} \times 10^{-13}$ erg cm^{-2} s^{-1}, $L_x = 4.9^{+0.3}_{-0.3} \times 10^{44}$ erg s^{-1}. Also in agreement with our above analysis of available *Chandra* data, we derive a total hydrogen column of $N_{H, tot} = 0.8^{+0.3}_{-0.3} \times 10^{22}$ cm^{-2} based on the *XMM–Newton* spectrum, of which $N_{H,X} = 0.5^{+0.2}_{-0.1} \times 10^{22}$ cm^{-2} is estimated to be intrinsic to PKS 1657−298.

4.4 Constraints from radio and X-rays

We consider here what constraint we can place on the physical properties of the galaxy based on the combination of our radio and X-ray data. To investigate the spin temperature, we take the same approach here as described in Allison et al. (2015), such that we can find an upper limit on spin temperature,

$$T_s \lesssim 5485 \left[\frac{N_{H,X}}{10^{22} \, \text{cm}^{-2}} \right] \left[\frac{\int \tau_{21} v \, dv}{1 \, \text{km s}^{-1}} \right]^{-1} \text{K}, \qquad (3)$$

where T_s is the spin temperature in K, $N_{H,X}$ is the total hydrogen column density as measured from the X-rays in cm^{-2} and $\int \tau_{21} v \, dv$ is the rest-frame velocity integrated optical depth. In the case of PKS 1657−298, $N_{H,X} = 0.6 \times 10^{22}$ cm^{-2} and $\int \tau_{21} v \, dv = 2.9$ km s^{-1}. Thus we find an upper limit for spin temperature of $T_s \lesssim 1130 \pm 380$ K, assuming a covering fraction of 1 based on the compactness seen on VLBI scales. Given that most H I absorbers have been found to have measured spin temperatures in the range 10^2–10^4 K (Curran 2012; Kanekar et al. 2014) as well as the predictions of higher spin temperatures near the central region of an AGN compared to standard Galactic spin temperatures (Bahcall & Ekers 1969), this result is entirely consistent with previous work.

Aside from the upper limit above (which is based on the assumption that $N_{H,X} = N_{HI}$), there are other factors to consider that will influence these measurements. First, since $N_{H,X}$ is a measure of the total hydrogen column, it will reflect the presence of neutral, ionized and molecular hydrogen while N_{HI} only probes the neutral hydrogen along the line of sight. So we would in all cases expect $N_{H,X} \geq N_{HI}$, but the relative fractions of ionized, neutral and molecular within the total $N_{H,X}$ would vary depending on the properties of the AGN and local interstellar medium. Given the results found by Wilson et al. (1998) of a low ionization fraction on the order of 10^{-2} to 10^{-5} in NGC 2639, it seems unlikely that the combination of ionized and molecular hydrogen could account for 90 per cent of the total hydrogen column. However, the AGN X-ray luminosity is three orders of magnitude brighter in the case of PKS 1657−298 than in NGC 2639 and thus it also seems extremely unlikely that the entire hydrogen column is neutral along the line of sight to the AGN. It is worth noting that for kinetic temperatures $T_k < 1000$ K in the cold neutral medium (CNM), T_s is basically equal to T_k (Liszt 2001; Roy, Chengalur & Srianand 2006), although the gas we detect towards the AGN may not be in the CNM phase due to its likely proximity to the central black hole. In any case, the true neutral fraction making up $N_{H,X}$ (likely located somewhere between 10–90 per cent) will thus lead to a lower spin temperature than the upper limit of ~ 1100 K.

We can consider the kinetic temperature implied by the line-width of our absorption line profile, as a means of comparing it to what we see in the spin temperature. We derive the kinetic temperature as in Moss et al. (2012), namely

$$T_k \leq \frac{m_H \sigma_v^2}{k}, \qquad (4)$$

where m_H is the mass of the hydrogen atom in kg, σ_v is the velocity dispersion of the line and k is the Boltzmann constant. Our measured FWHM line-width for PKS 1657−298 is 63 km s^{-1}, which
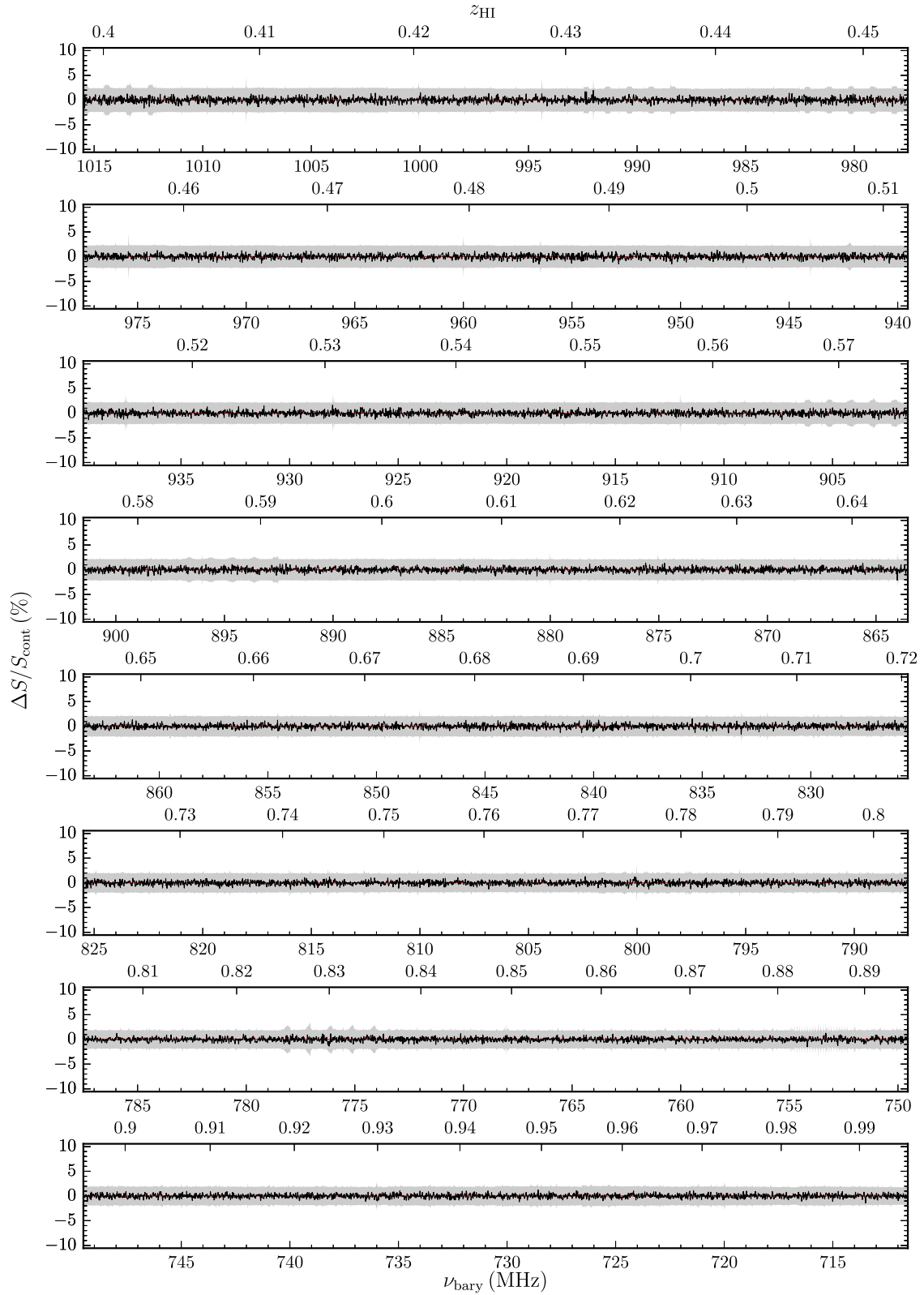
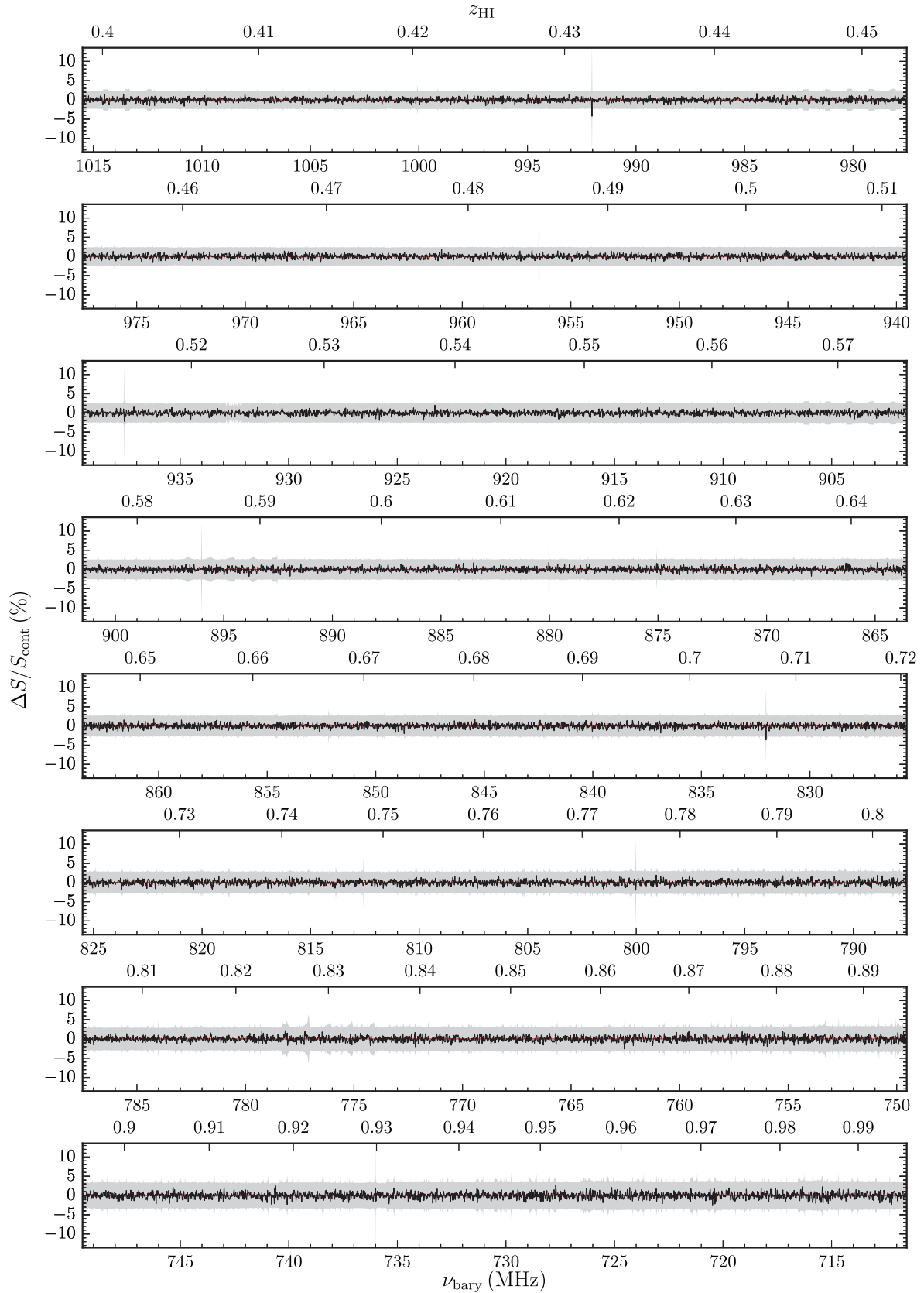**Figure 16.** Averaged ASKAP–BETA spectrum for PKS 1547−79 based on 8 hr of observations. The sensitivity of this averaged spectrum is 23 mJy beam^{-1}, corresponding to a 5σ optical depth sensitivity of $\tau > 0.019$. In this figure, and each figure following, the grey region represents the 5σ noise level in that channel.
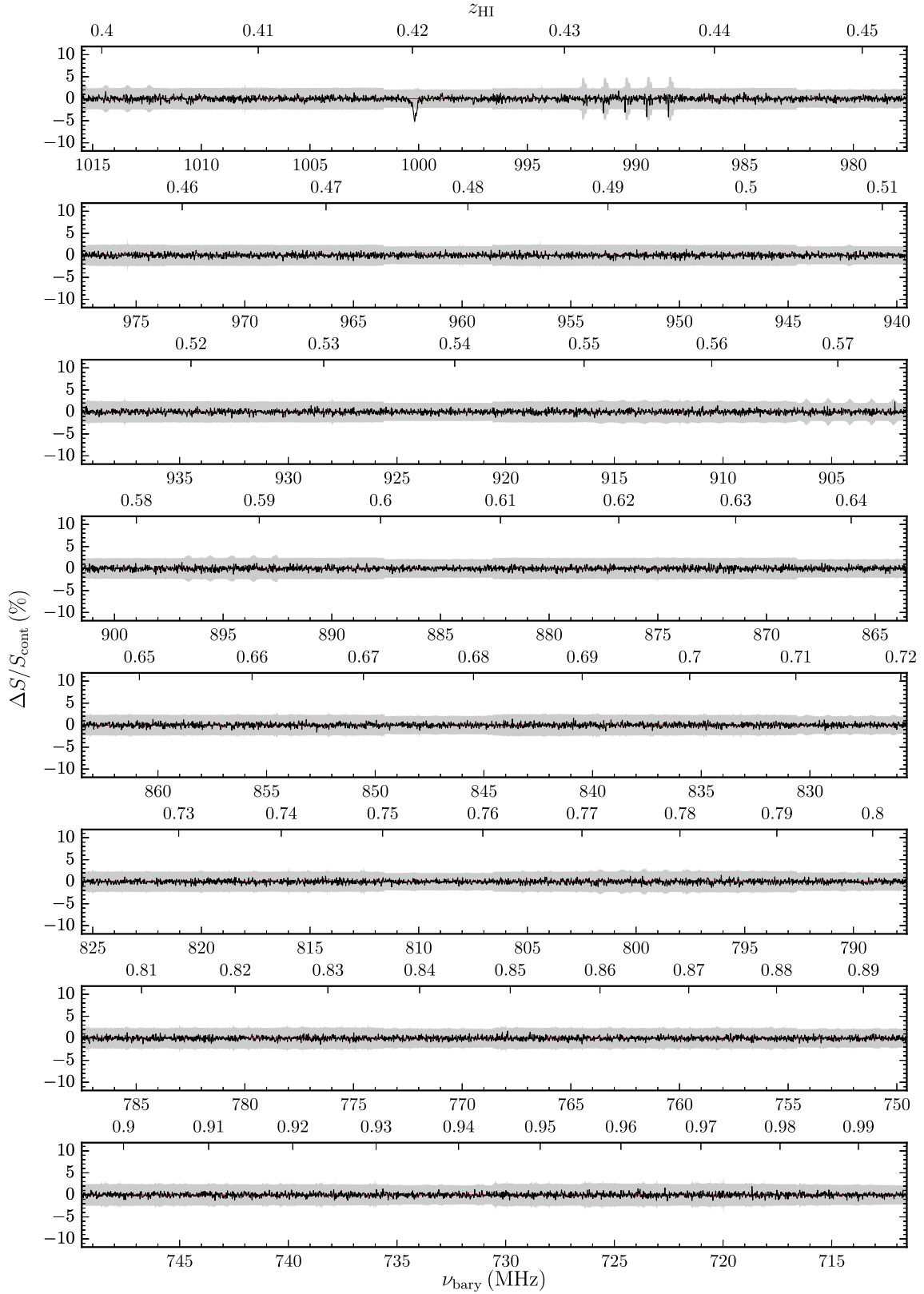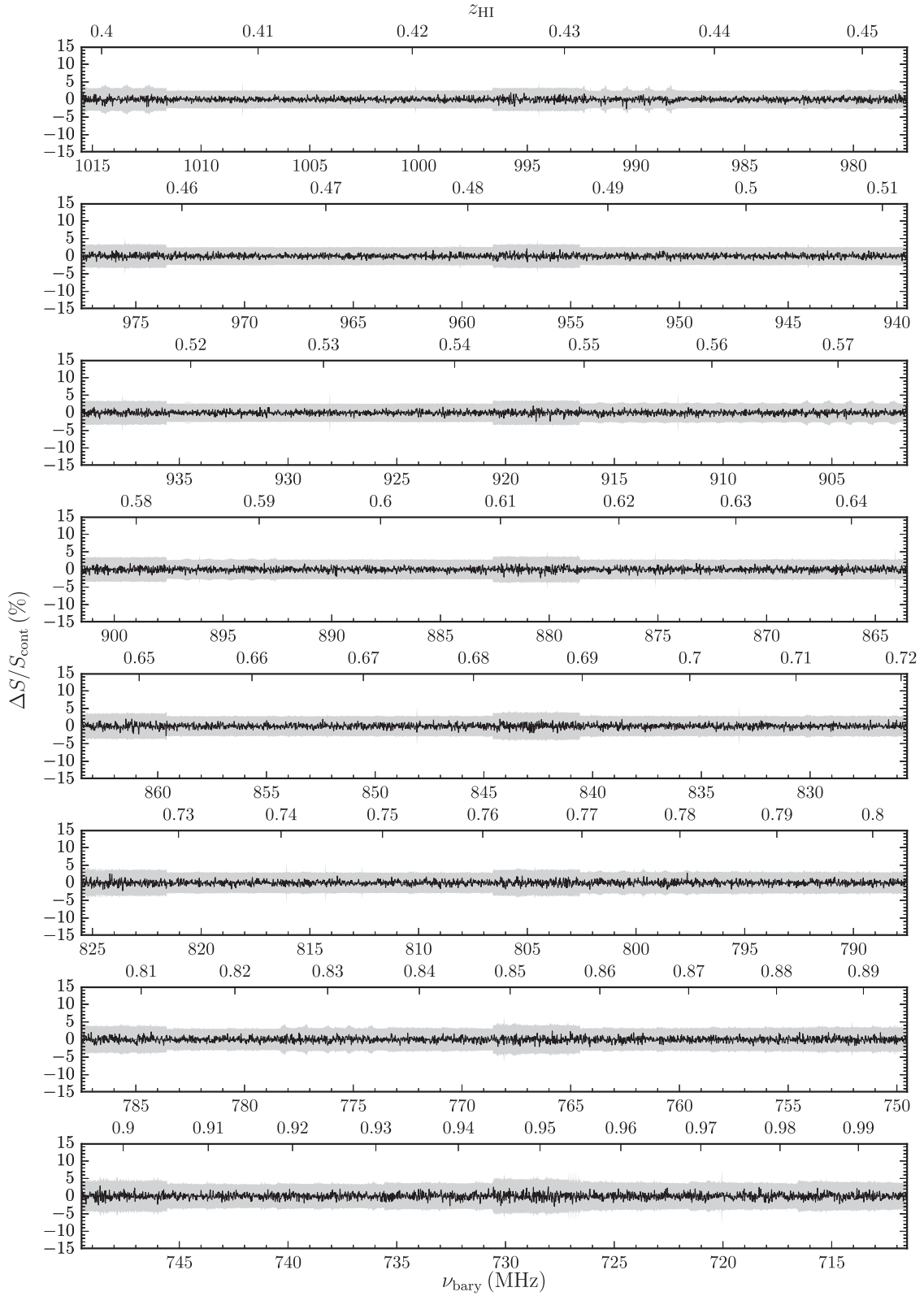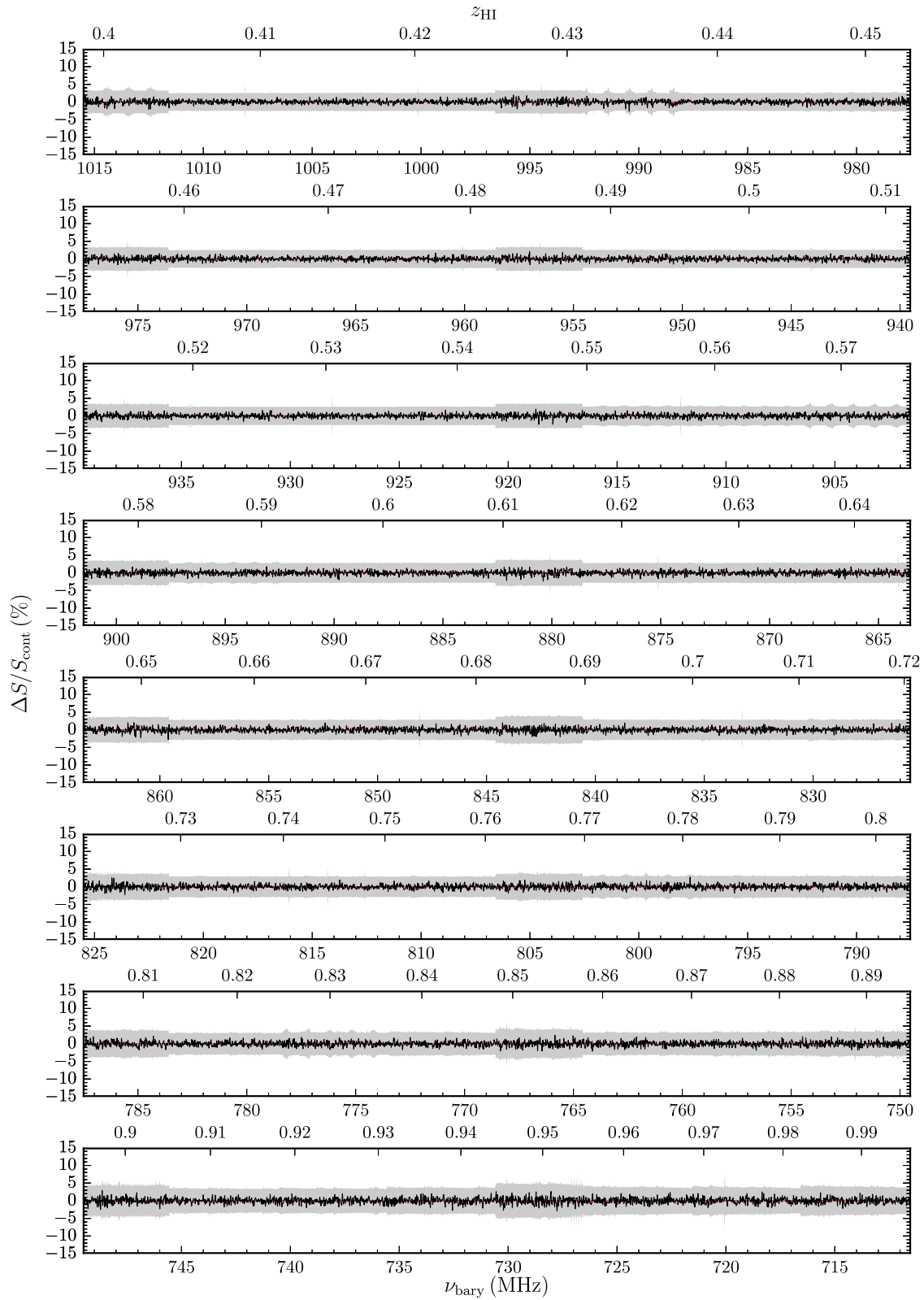
Figure 17. Averaged ASKAP–BETA spectrum for PKS 1657−298 based on 27.25 hr of observations. The sensitivity of this averaged spectrum is 11 mJy beam^{-1}, corresponding to a 5σ optical depth sensitivity of $\tau > 0.022$.

Figure 18. Averaged ASKAP–BETA spectrum for MRC 1722−644 based on 3 hr of observations. The sensitivity of this averaged spectrum is 29 mJy beam^{-1}, corresponding to a 5σ optical depth sensitivity of $\tau > 0.032$.

Figure 19. Averaged ASKAP–BETA spectrum for PKS 2008−068 based on 15.5 hr of observations. The sensitivity of this averaged spectrum is 17 mJy beam^{-1}, corresponding to a 5σ optical depth sensitivity of $\tau > 0.028$. An increase in noise is seen at regular intervals throughout the spectrum (every 4 chunks, e.g. at 1015 MHz) due to correlator issues, resulting in a reduced optical depth sensitivity of $\tau > 0.05$ in this part of the spectrum. We note that the reported redshift of the host galaxy ($z = 0.547$) does correspond to one of these affected chunks.

Figure 20. Averaged ASKAP–BETA spectrum for PKS 2154−11 based on 13.2 hr of observations. The sensitivity of this averaged spectrum is 22 mJy beam^{-1}, corresponding to a 5σ optical depth sensitivity of $\tau > 0.070$.

corresponds to a σ_v of 27 km s^{-1}. This gives an upper limit estimate for T_k of 8.6×10^4 K, however we note that this does not take into account the effects of rotation or turbulent broadening both of which will result in a non-thermally broadened line. It is possible that including these effects could reduce the width of the line by the factor of ∼60 required to match the spin temperature upper limit.

It is also important to note the assumption made above that the H I and X-rays are spatially coincident. There is no guarantee based on these data that we are probing the same physical regions that we see in H I absorption and in X-ray absorption. While we might expect the X-ray emission to arise from a reasonably uniform area surrounding the torus of the AGN, it remains unclear whether the H I absorption we see arises from a similarly uniform region or if it instead comes from a clumpy region and we are detecting cold clouds along the line of sight (e.g. as in the case of Maccagni et al. 2014). However, our results here showing that H I absorbers are more likely to feature significant soft X-ray absorption support the suggestion of co-spatiality, alongside the results presented by Ostorero et al. (2010) of a tentative but statistically robust positive correlation between $N_{H,X}$ and N_{HI}. Further data in this area, as well as detailed information on more comparable spatial scales (i.e. through VLBI studies of the H I absorption distribution in associated systems), will be key in conclusively answering this question of spatial coincidence.

5 CONCLUSION

We have presented here analysis of the radio and X-ray properties of 94 galaxies searched for H I absorption, including 20 absorbers and 74 non-detections. By analysing their X-ray properties, we find that absorbers are more likely to feature an absorbed X-ray spectrum. We also find a statistically significant trend at 4.71σ using survival analysis indicating correlation between H I optical depth and X-ray hardness, as well as a higher proportion of absorbers with increasing X-ray hardness. These results are all supportive of correlation between H I absorption and soft X-ray absorption and are strongly suggestive that these absorption mechanisms are tracing similarly distributed populations of gas. In future investigations, we plan to further explore this correlation in order to confirm the spatial distribution of N_{HI} and N_H, and determine whether we are detecting absorption from inside the sphere of influence of the black hole (probing a torus or wind), from a few 10 s of pc in the galactic nucleus (probing the galactic inflow and of the gas available for black hole growth), or a few kpc in the whole galaxy (probing the large-scale galaxy evolution). More detailed analysis and complex modelling of high signal-to-noise X-ray spectra where available, in comparison with studies in the literature (e.g. Buchner & Bauer 2017), will aid in separating galactic-scale from nuclear-scale absorption contributions.

We have also presented the results of a pilot study conducted with the commissioning telescope BETA, as part of preparations for FLASH science with ASKAP. Our sample of five X-ray absorbed galaxies revealed a new H I absorption detection at a redshift of $z = 0.42$, towards PKS 1657−298, which also showed the most X-ray absorption in its 3XMM-DR4 catalogue spectrum. PKS 1657−298 is detected across the electromagnetic spectrum, particularly at mid-infrared wavelengths as seen in WISE data. Although we do not currently have an optical spectroscopic confirmation of the radio source redshift, the *K-z* relation based on analysis by Willott et al. (2003) is consistent with the redshift as measured in H I. In analysing the properties of the H I absorption towards PKS

1657−298, we find values of optical depth $\tau = 0.046$, effective line width, $\Delta v_{eff} = 63$ km s^{-1} and $N_{HI} = 5.3 \times 10^{20}$ cm^{-2}, assuming a spin temperature of 100 K and a covering fraction of 1.

Our analysis of archival *XMM–Newton* and *Chandra* data for PKS 1657−298 reveals consistent results for intrinsic X-ray luminosity $L_x \sim 5 \times 10^{44}$ erg s^{-1} and an estimated hydrogen column density in the galaxy of $N_{H,X} \sim 6 \times 10^{21}$ cm^{-2}. In the *Chandra* data, a simple absorbed power-law model is not sufficient to take into account high-energy residuals, which are instead well-fit by assuming the presence of both a narrow 6.4 keV Fe line and a 7.1 keV Fe K-shell absorption edge both at a redshift of $z = 0.42$. The *XMM–Newton* data does not have high enough signal to noise to confirm this, but the data are statistically consistent with the results from *Chandra*. We conclude that this is the most likely scenario for interpreting the high-energy components we see in our averaged spectra, however we note that we cannot currently distinguish these from a P-Cygni profile signifying an outflow in the host galaxy. The combination of X-ray absorption with H I absorption allows us to place an upper limit on the spin temperature of gas in PKS 1657−298 of $T_s \lesssim 1130 \pm 380$ K.

Our X-ray pilot sample has shown the potential for expanding this line of investigation with ASKAP Early Science and beyond, as well as with telescopes around the world able to explore neutral gas at these intermediate redshifts. The BETA sample was extremely limited in sensitivity to sources above 1 Jy, however with full ASKAP we will have access to the radio source population down to ∼50 mJy which opens up an entire new window on the parameter space we can explore. There is particularly strong synergy between the H I absorption population to be discovered with FLASH and the all-sky survey capability in X-rays of *eROSITA* (Merloni et al. 2012), where we expect to greatly expand on the results described here. It is also critical to further explore the question of spatial correlation between X-rays and radio emission near the core of radio galaxies, which will be made possible in the Southern hemisphere with extension of VLBI capability to lower frequencies using baselines between ASKAP and the 0.7–4 GHz wide-band receiver of the Parkes telescope (Manchester 2015). In the more distant future, the powerful combination of the Square Kilometre Array (Dewdney et al. 2009) with *Athena* (Barret et al. 2013) will enable studies of these objects at sensitivities that are orders of magnitude beyond what we can currently achieve with existing telescopes, up to $z = 3$ and across a much wider range of galaxy types, luminosities and evolutionary states.

REFERENCES

Allison J. R. et al., 2012, MNRAS, 423, 2601
Allison J. R. et al., 2015, MNRAS, 453, 1249
Allison J. R. et al., 2016, MNRAS, 456, 3030
Allison J. R. et al., 2017, MNRAS, 465, 4450
Arnaud K. A., 1996, in Jacoby G. H., Barnes J., eds, ASP Conf. Ser. Vol. 101, Astronomical Data Analysis Software and Systems V. Astron. Soc. Pac., San Francisco, p. 17
Bahcall J. N., Ekers R. D., 1969, ApJ, 157, 1055
Barret D. et al., 2013, in Cambresy L., Martins F., Nuss E., Palacios A., eds, Proc. Annu. Meeting French Soc. Astron. Astrophys., SF2A-2013. p. 447
Berge G. L., Seielstad G. A., 1972, AJ, 77, 810
Buchner J., Bauer F. E., 2017, MNRAS, 465, 4348
Burgess A. M., Hunstead R. W., 2006, AJ, 131, 114
Callingham J. R. et al., 2015, ApJ, 809, 168
Callingham J. R. et al., 2016, MNRAS, 462, 290
Carilli C. L., Menten K. M., Reid M. J., Rupen M. P., Yun M. S., 1998, ApJ, 494, 175
Cava A. et al., 2009, A&A, 495, 707
Chandola Y., Sirothia S. K., Saikia D. J., 2011, MNRAS, 418, 1787
Chandola Y., Gupta N., Saikia D. J., 2013, MNRAS, 429, 2380
Collaboration A. et al., 2013, A&A, 558, A33
Condon J. J., Cotton W. D., Greisen E. W., Yin Q. F., Perley R. A., Taylor G. B., Broderick J. J., 1998, AJ, 115, 1693
Curran S. J., 2012, ApJL, 748, L18
Curran S. J., 2017, preprint (arXiv:1704.04294)
Curran S. J., Whiting M. T., 2010, ApJ, 712, 303
Curran S. J., Whiting M. T., Wiklind T., Webb J. K., Murphy M. T., Purcell C. R., 2008, MNRAS, 391, 765
Curran S. J., Whiting M. T., Allison J. R., Tanna A., Sadler E. M., Athreya R., 2017, MNRAS, 467, 4514
Dewdney P. E., Hall P. J., Schilizzi R. T., Lazio T. J. L. W., 2009, Proc. IEEE, 97, 1482
di Serego-Alighieri S., Danziger I. J., Morganti R., Tadhunter C. N., 1994, MNRAS, 269, 998
Douglas J. N., Bash F. N., Bozyan F. A., Torrence G. W., Wolfe C., 1996, AJ, 111, 1945
Doyle M. T. et al., 2005, MNRAS, 361, 34
Duncan R. A., Sproats L. N., 1992, Proc. Astron. Soc. Aust., 10, 16
Edwards P. G., Tingay S. J., 2004, A&A, 424, 91
Edwards P. G., Tingay S. J., 2016, Publ. Astron. Soc. Aust., 33, e060
Emonts B. H. C. et al., 2010, MNRAS, 406, 987
Fabian A. C., 2012, ARA&A, 50, 455
Fanti C., Fanti R., Dallacasa D., Schilizzi R. T., Spencer R. E., Stanghellini C., 1995, A&A, 302, 317
Feigelson E. D., Nelson P. I., 1985, ApJ, 293, 192
Gardner F. F., Davies R. D., 1966, Aust. J. Phys., 19, 441
Gereb K., Maccagni F. M., Morganti R., Oosterloo T. A., 2015, A&A, 575, A44
Glowacki M. et al., 2017, MNRAS, 467, 2766
Greenhill L. J., Moran J. M., Herrnstein J. R., 1997, ApJ, 481, L23
Gupta N., Salter C. J., Saikia D. J., Ghosh T., Jeyakumar S., 2006, MNRAS, 373, 972
Haardt F., Maraschi L., 1993, ApJ, 413, 507
Hambly N. C. et al., 2001, MNRAS, 326, 1279
Heckman T. M., Best P. N., 2014, ARA&A, 52, 589
Holt J., Tadhunter C. N., Morganti R., 2008, MNRAS, 387, 639
Hotan A. W. et al., 2014, Publ. Astron. Soc. Aust., 31, e041
Hurley-Walker N. et al., 2017, MNRAS, 464, 1146
Inoue M., Tabara H., Kato T., Aizu K., 1995, PASJ, 47, 725
Intema H. T., Jagannathan P., Mooley K. P., Frail D. A., 2017, A&A, 598, A78
Isobe T., Feigelson E. D., Nelson P. I., 1986, ApJ, 306, 490
Johnson R. E., Markevitch M., Wegner G. A., Jones C., Forman W. R., 2010, ApJ, 710, 1776
Johnston K. J. et al., 1995, AJ, 110, 880
Johnston S. et al., 2007, Publ. Astron. Soc. Aust., 24, 174
Kanekar N. et al., 2014, MNRAS, 438, 2131
Koribalski B. S. et al., 2004, AJ, 128, 16
Kuehr H., Witzel A., Pauliny-Toth I. I. K., Nauber U., 1981, A&A, 45, 367
Lane W. M., Cotton W. D., van Velzen S., Clarke T. E., Kassim N. E., Helmboldt J. F., Lazio T. J. W., Cohen A. S., 2014, MNRAS, 440, 327
Large M. I., Mills B. Y., Little A. G., Crawford D. F., Sutton J. M., 1981, MNRAS, 194, 693
Lasker B. M., Sturch C. R., McLean B. J., Russell J. L., Jenkner H., Shara M. M., 1990, AJ, 99, 2019
Lavalley M., Isobe T., Feigelson E., 1992, in Worrall D. M., Biemesderfer C., Barnes J., eds, ASP Conf. Ser. Vol. 25, Astronomical Data Analysis Software and Systems I. Astron. Soc. Pac., San Francisco, p. 245
Lilly S. J., Longair M. S., 1984, MNRAS, 211, 833
Liszt H., 2001, A&A, 371, 698
Maccagni F. M., Morganti R., Oosterloo T. A., Mahony E. K., 2014, A&A, 571, A67
Maccagni F. M., Morganti R., Oosterloo T. A., Geréb K., Maddox N., 2017, preprint (arXiv:1705.00492)
Madau P., Dickinson M., 2014, ARA&A, 52, 415
Magdziarz P., Zdziarski A. A., 1995, MNRAS, 273, 837
Mahony E. K. et al., 2011, MNRAS, 417, 2651
Manchester R. N., 2015, IAU General Assembly, Meeting, 22, 2256190
Mauch T., Murphy T., Buttery H. J., Curran J., Hunstead R. W., Piestrzynski B., Robertson J. G., Sadler E. M., 2003, MNRAS, 342, 1117
McConnell D. et al., 2016, Publ. Astron. Soc. Aust., 33, e042
McLean B. J., Greene G. R., Lattanzi M. G., Pirenne B., 2000, in Manset N., Veillet C., Crabtree D., eds, ASP Conf. Ser. Vol. 216, Astronomical Data

Analysis Software and Systems IX. Astron. Soc. Pac., San Francisco, p. 145

Merloni A., Heinz S., Di Matteo T., 2003, MNRAS, 345, 1057

Merloni A. et al., 2012, preprint (arXiv:1209.3114)

Mingo B., Hardcastle M. J., Croston J. H., Dicken D., Evans D. A., Morganti R., Tadhunter C., 2014, MNRAS, 440, 269

Morganti R., Oosterloo T. A., Tadhunter C. N., Van Moorsel G., Killeen N., Wills K. A., 2001, MNRAS, 323, 331

Morganti R., Sadler E. M., Curran S., 2015, Proc. Sci., Cool Outflows and HI absorbers with SKA. SISSA, Trieste, PoS#134

Moss V. A., McClure-Griffiths N. M., Braun R., Hill A. S., Madsen G. J., 2012, MNRAS, 421, 3159

Murphy T. et al., 2010, MNRAS, 402, 2403

Nardini E. et al., 2015, Science, 347, 860

Nelder J. A., Mead R., 1965, Comput. J., 7, 308

Noterdaeme P. et al., 2012, A&A, 547, L1

O'Dea C. P., 1998, Publ. Astron. Soc. Aust., 110, 493

Orienti M., Morganti R., Dallacasa D., 2006, A&A, 457, 531

Ostorero L. et al., 2010, ApJ, 715, 1071

Petrov L., Honma M., Shibata S. M., 2012, AJ, 143, 35

Pounds K. A., Reeves J. N., 2009, MNRAS, 397, 249

Ramos Almeida C., Tadhunter C. N., Inskip K. J., Morganti R., Holt J., Dicken D., 2011, MNRAS, 410, 1550

Reynolds C. S., 2016, Astron. Nachr., 337, 404

Rosen S. et al., 2015, in Taylor A. R., Rosolowsky E., eds, ASP Conf. Ser. Vol. 495, Astronomical Data Analysis Software an Systems XXIV (ADASS XXIV). Astron. Soc. Pac., San Francisco, p. 319

Röttgering H., de Bruyn G., Pentericci L., 1999, in Röttgering H. J. A., Best P. N., Lehnert M. D., eds, The Most Distant Radio Galaxies. Royal Netherlands Academy of Arts and Sciences, p. 113

Roy N., Chengalur J. N., Srianand R., 2006, MNRAS, 365, L1

Siemiginowska A., LaMassa S., Aldcroft T. L., Bechtold J., Elvis M., 2008, ApJ, 684, 811

Skrutskie M. F. et al., 2006, AJ, 131, 1163

Snellen I. A. G., Schilizzi R. T., de Bruyn A. G., Miley G. K., Rengelink R. B., Roettgering H. J., Bremer M. N., 1998, A&AS, 131, 435

Snellen I. A. G., Lehnert M. D., Bremer M. N., Schilizzi R. T., 2002, MNRAS, 337, 981

Stanghellini C., O'Dea C. P., Dallacasa D., Baum S. A., Fanti R., Fanti C., 1998, A&AS, 131, 303

Tadhunter C., 2016, A&AR, 24, 10

Tadhunter C. N., Morganti R., di Serego-Alighieri S., Fosbury R. A. E., Danziger I. J., 1993, MNRAS, 263, 999

Tingay S. J. et al., 2013, Publ. Astron. Soc. Aust., 30, e007

Tinti S., De Zotti G., 2006, A&A, 445, 889

Turner T. J., Miller L., 2009, A&AR, 17, 47

Uson J. M., Bagri D. S., Cornwell T. J., 1991, Phys. Rev. Lett., 67, 3328

van Gorkom J. H., Knapp G. R., Ekers R. D., Ekers D. D., Laing R. A., Polk K. S., 1989, AJ, 97, 708

Verbunt F., 2001, A&A, 368, 137

Vermeulen R. C. et al., 2003, A&A, 404, 861

Vink J., Snellen I., Mack K.-H., Schilizzi R., 2006, MNRAS, 367, 928

Wayth R. B. et al., 2015, Publ. Astron. Soc. Aust., 32, e025

Willingale R., Starling R. L. C., Beardmore A. P., Tanvir N. R., O'Brien P. T., 2013, MNRAS, 431, 394

Willott C. J., Rawlings S., Jarvis M. J., Blundell K. M., 2003, MNRAS, 339, 173

Wilms J., Allen A., Mccray R., 2000, ApJ, 542, 914

Wilson A. S. et al., 1998, ApJ, 505, 587

Worrall D. M., 2009, A&AR, 17, 1

Wright E. L. et al., 2010, AJ, 140, 1868

This paper has been typeset from a TEX/LATEX file prepared by the author.